Title

Cancer-cell-secreted exosomal miR-105 promotes tumour growth through the MYC-dependent metabolic reprogramming of stromal cells.

Journal

Nature cell biology, 20(5)

ISSN

1465-7392

Authors

Yan, Wei
Wu, Xiwei
Zhou, Weiying
et al.

Publication Date

2018-05-01

DOI

10.1038/s41556-018-0083-6

Peer reviewed

nature cell biology

ARTICLES

https://doi.org/10.1038/s41556-018-0083-6

Cancer-cell-secreted exosomal miR-105 promotes tumour growth through the MYC-dependent metabolic reprogramming of stromal cells

Wei Yan[1], Xiwei Wu[2], Weiying Zhou[3,4], Miranda Y. Fong[1,3], Minghui Cao[1], Juan Liu[5], Xiaojing Liu[5], Chih-Hong Chen[6], Oluwole Fadare[1], Donald P. Pizzo[1], Jiawen Wu[1], Liang Liu[7], Xuxiang Liu[8], Andrew R. Chin[1,8], Xiubao Ren[7], Yuan Chen[6], Jason W. Locasale[5] and Shizhen Emily Wang[1,9*]

Cancer and other cells residing in the same niche engage various modes of interactions to synchronize and buffer the negative effects of environmental changes. Extracellular microRNAs (miRNAs) have recently been implicated in the intercellular crosstalk. Here we show a mechanistic model involving breast-cancer-secreted, extracellular-vesicle-encapsulated miR-105, which is induced by the oncoprotein MYC in cancer cells and, in turn, activates MYC signalling in cancer-associated fibroblasts (CAFs) to induce a metabolic program. This results in the capacity of CAFs to display different metabolic features in response to changes in the metabolic environment. When nutrients are sufficient, miR-105-reprogrammed CAFs enhance glucose and glutamine metabolism to fuel adjacent cancer cells. When nutrient levels are low and metabolic by-products accumulate, these CAFs detoxify metabolic wastes, including lactic acid and ammonium, by converting them into energy-rich metabolites. Thus, the miR-105-mediated metabolic reprogramming of stromal cells contributes to sustained tumour growth by conditioning the shared metabolic environment.

Cancer engages a dynamic interplay among cells in the cancer-hosting niche[1,2]. Across the many levels of intercellular crosstalk, a role for cancer-secreted extracellular vesicles (EVs) has been recognized[3,4]. Through travelling in the interstitial spaces and blood, EVs transfer biomolecules between adjacent or distant cells[5–7]. Cancer-derived EVs are implicated in tissue invasion, angiogenesis, immune evasion and metastasis[7–15], with many of these functions attributed to EV-encapsulated microRNA (miRNA) post-transcriptionally regulating gene expression in niche cells[16–18]. We previously reported that breast cancer (BC) cells secrete miR-105 to destroy tight junctions in vascular endothelial cells and promote metastasis[11], and that BC-secreted miR-122 suppresses glucose utilization in a pre-metastatic niche to outsmart nutrient competition[10]. Increased levels of circulating miR-105 and miR-122 can be detected at a pre-metastatic stage and correlate with the occurrence of metastasis in BC patients; systemic interventions of these miRNAs suppress BC metastases[10,11,19]. Here, we extend our study of cancer-secreted miRNA to the metabolic reprogramming of cancer-associated fibroblasts (CAFs), a major cellular component of tumour stroma[20].

Proliferative cancer cells often acquire enhanced abilities to exploit nutrients, such as glucose and glutamine, to support their energy demand and biomass synthesis[21–23]. This, along with the generation of metabolic by-products including lactic acid (LA; from aerobic glycolysis known as the Warburg effect) and ammonium (NH_4^+), influences the metabolic environment of tumour-milieu-residing niche cells, highlighting the necessity to rebalance the metabolic needs of cancer and niche cells. Interestingly, in some tumours, CAFs are also found to undergo aerobic glycolysis[24,25], and may secrete energy-rich metabolites such as pyruvate and lactate to fuel neighbouring cancer cells[26,27]. Expression of monocarboxylate transporter (MCT) 4 in tumour stroma is associated with progression to invasive BC, suggesting a role for MCT-dependent stroma-to-cancer metabolite transfer[28]. However, this model requires adequate glucose to suffice both glycolytic cancer cells and CAFs, to enable a pro-cancerous metabolic interplay rather than provoking a competition between the two cell populations. When the environment is deprived of nutrients, which is a common intermittent stress in a growing tumour often concurring with accumulation of metabolic wastes due to insufficient vascular drainage, CAFs may undergo a different metabolic interplay with cancer cells that is yet to be elucidated. We therefore set out to unravel the complex metabolic interactions between BC cells and CAFs.

Results

miR-105 induces a MYC-dependent metabolic program. Patient-derived CAFs[29] (Supplementary Fig. 1) exhibited high and comparable uptake efficiencies for EVs from MDA-MB-231 BC cells and MCF10A non-cancer cells (Fig. 1a). RNA-seq transcriptome profiling followed by gene set enrichment analysis (GSEA) revealed enrichment of a gene signature related to MYC activation in CAFs treated with MDA-MB-231 EVs compared to those receiving MCF10A EVs or PBS (Fig. 1b). In search of the potential upstream event leading to MYC activation, we observed >50% downregulation

[1]Department of Pathology, University of California San Diego, La Jolla, CA, USA. [2]Department of Molecular and Cellular Biology, Beckman Research Institute of City of Hope, Duarte, CA, USA. [3]Department of Cancer Biology, Beckman Research Institute of City of Hope, Duarte, CA, USA. [4]School of Pharmacy, Chongqing Medical University, Chongqing, China. [5]Department of Pharmacology and Cancer Biology, Duke University, Durham, NC, USA. [6]Department of Molecular Medicine, Beckman Research Institute of City of Hope, Duarte, CA, USA. [7]Department of Immunology and Biotherapy, Tianjin Medical University Cancer Institute and Hospital, Tianjin, China. [8]City of Hope Irell & Manella Graduate School of Biological Sciences, Duarte, CA, USA. [9]Moores Cancer Center, University of California San Diego, La Jolla, CA, USA. *e-mail: emilywang@ucsd.edu

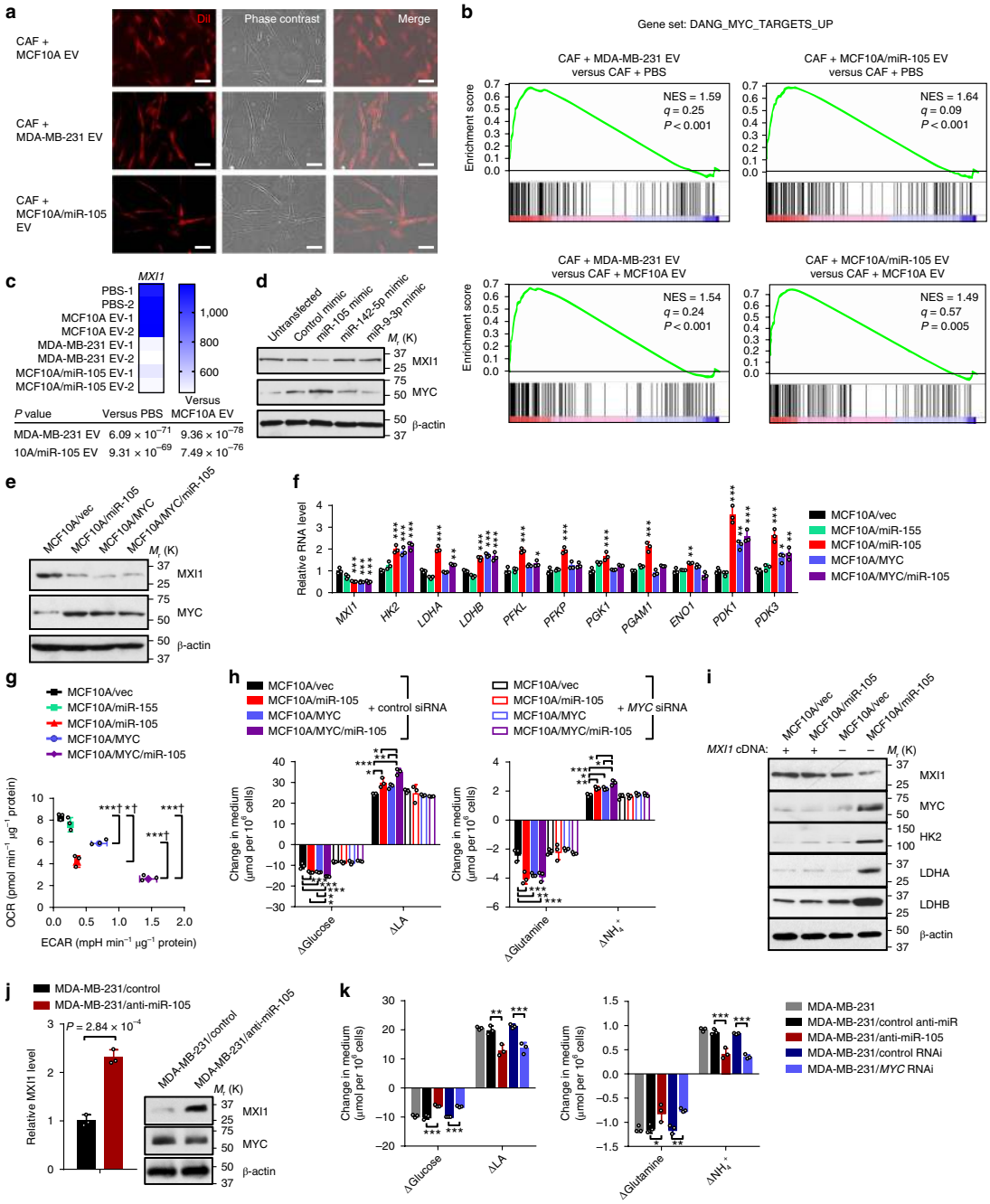

Fig. 1 | miR-105 induces a MYC-dependent metabolic program. a, CAFs were incubated with DiI-labelled EVs (red) for 24 h before fluorescent and phase-contrast images were captured. Scale bars, 100 μm. The experiment was repeated independently three times with similar results. **b**, GSEA demonstrating the enrichment of a MYC target gene set in CAFs treated with MDA-MB-231 EVs or MCF10A/miR-105 EVs versus those treated with PBS or MCF10A EVs. On the basis of data from two independent replicates, genes were ranked by the signed *P* value score from edgeR (see Methods) and subjected to GSEA interrogation, which generated the indicated *P* value, *q* value and normalized enrichment score (NES) for each gene set based on 1,000 random permutations. **c**, Heat map showing the normalized counts of *MXI1* in all CAF RNA samples (exact test by edgeR, $n = 2$ independent experiments). The *P* value was calculated by edgeR using an exact test. **d**, Western blots showing the expression levels of the indicated protein miRNA-mimic-transfected CAFs. **e**, Western blots showing the expression levels of the indicated proteins in MCF10A cells overexpressing miR-105 or MYC, or both. **f**, Relative RNA levels detected by quantitative PCR with reverse transcription (RT–qPCR) and compared to the MCF10A/vec cells (one-way analysis of variance (ANOVA), $n = 3$ independent experiments). **g**, Extracellular acidification rate (ECAR) and oxygen consumption rate (OCR) assays in MCF10A cells overexpressing the empty vector, miR-155, miR-105, MYC or both miR-105 and MYC (one-way ANOVA, $n = 3$ independent experiments). *ECAR $P < 0.05$, ***ECAR $P < 0.001$, †OCR $P < 0.001$. **h**, Changes in metabolite levels in the medium within 72 h in the indicated cells transfected with *MYC* short interfering RNA (siRNA, right) or control siRNA (left) (one-way ANOVA, $n = 3$ independent experiments). **i**, Western blots showing the expression levels of the indicated proteins in MCF10A cells with or without miR-105 overexpression and previously transfected with an expression plasmid of *MXI1* complementary DNA lacking the 3′UTR or a control vector. **j**, RNA and protein levels of MXI1 in MDA-MB-231 cells transfected with anti-miR-105 or control (two-sided *t*-test, $n = 3$ independent experiments). **k**, Changes in metabolite levels in the medium over 72 h by MDA-MB-231 cells treated as indicated (one-way ANOVA, $n = 3$ independent experiments). In all panels, the data are shown as mean ± s.d.; *$P < 0.05$, **$P < 0.01$, ***$P < 0.001$. Unprocessed original scans of blots are shown in Supplementary Fig. 9. Source data are shown in Supplementary Table 5.

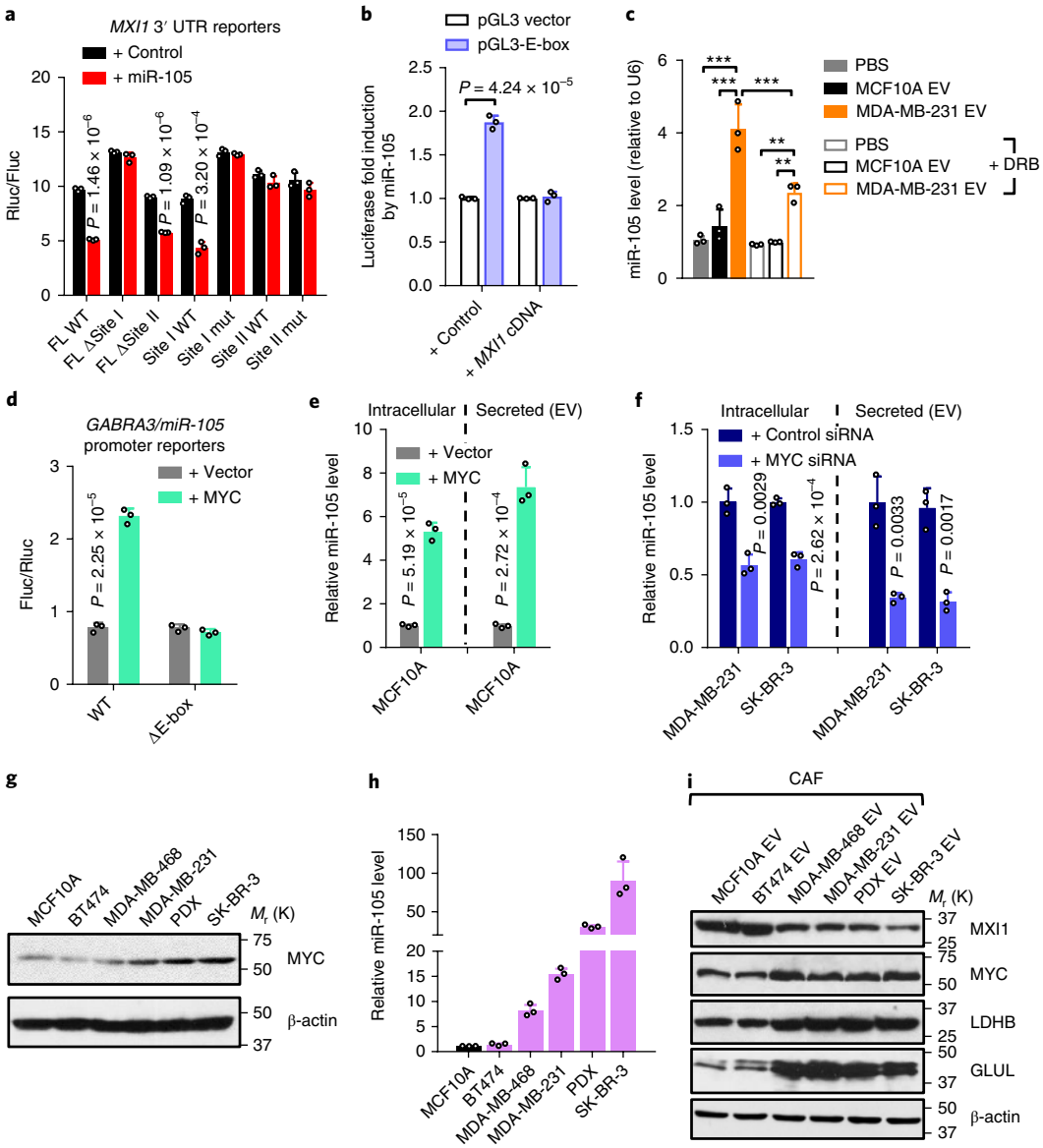

Fig. 2 | miR-105 targets *MXI1* to activate MYC signalling and is induced by MYC. a, Responsiveness of the WT and mutant MXI1 3′ UTR reporters (shown in Supplementary Fig. 4a) to a miR-105 mimic in transfected MCF10A cells, as indicated by the ratio of *Renilla* luciferase (Rluc) to firefly luciferase (Fluc) (two-sided *t*-test, $n=3$ independent experiments). **b**, Responsiveness of an E-box reporter and the control reporter to a miR-105 mimic in the absence or presence of ectopic expression of *MXI1* cDNA lacking the 3′ UTR (two-sided *t*-test, $n=3$ independent experiments). **c**, MCF10A- or MDA-MB-231-secreted EVs were fed to CAFs in the presence or absence of DRB (5,6-dichloro-1-β-D-ribofuranosylbenzimidazole; 20 μM). After 24 h, RNA extracted from the recipient cells was analysed for miR-105 level using U6 as an internal reference (one-way ANOVA, $n=3$ independent experiments). **d**, Responsiveness of WT and mutant *miR-105* promoter reporters to a MYC expression vector in transfected MCF10A cells (two-sided *t*-test, $n=3$ independent experiments). **e**,**f**, Levels of miR-105 in cells (normalized to U6) and EVs (normalized to the cel-miR-39-3p spike-in control) under *MYC* overexpression (**e**) or siRNA knockdown for 24 h (**f**) (two-sided *t*-test, $n=3$ independent experiments). **g**, Western blots showing protein levels in the indicated non-cancerous breast cells (MCF10A) and BC cells. **h**, RT–qPCR-determined levels of miR-105 in equal amounts of EVs from the indicated cells (normalized to the cel-miR-39-3p spike-in control; $n=3$ independent experiments). **i**, Western blots showing expression levels of the indicated proteins in CAFs treated with equal amounts of EVs from the indicated cells. For all panels, the data are shown as mean ± s.d.; $^{**}P<0.01$, $^{***}P<0.001$. Unprocessed original scans of blots are shown in Supplementary Fig. 9. Source data are shown in Supplementary Table 5.

of the gene encoding MXI1 (MAX-interacting protein 1) (Fig. 1c), a protein that antagonizes the MYC–MAX dimeric transcriptional factor through forming heterodimers with MAX[30], recruiting transcription repressors[31,32] and directly suppressing transcription from the *MYC* promoter[33]. Eight miRNAs are predicted by three independent algorithms to recognize the 3′untranslated region (UTR) of *MXI1*; among these, we focused on miR-105 because of its highest cancer-versus-normal secretion with an undetectable level in MCF10A EVs (Supplementary Table 1), its capacity to decrease MXI1 and elevate MYC protein levels in CAFs (Fig. 1d) and its association with BC progression[11]. Indeed, EVs from MCF10A cells engineered to overexpress and secrete miR-105 also induced the MYC activation gene signature and downregulated *MXI1* in CAFs (Fig. 1b,c). Characterization of EVs by nanoparticle tracking analysis and density gradient fractionation indicated enrichment of miR-105 in exosome-containing fractions (Supplementary Fig. 2).

Gene expression associated with miR-105 overexpression in MCF10A cells revealed enrichment of gene sets related to MYC activation

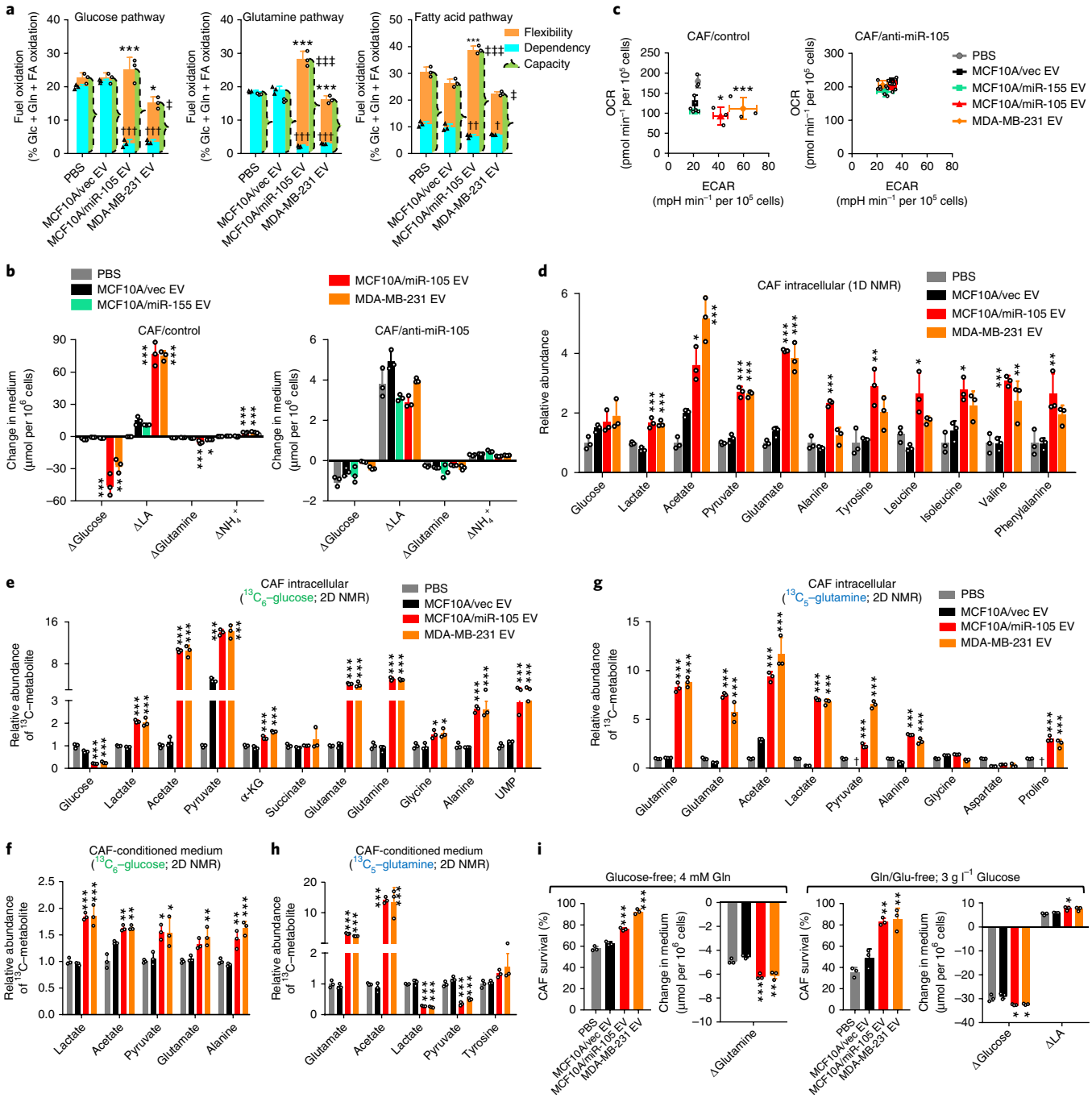

Fig. 3 | CAFs are reprogrammed by cancer-secreted miR-105 to enhance secretion of glucose- and glutamine-derived metabolites. a, Mitochondrial fuel test to determine the flexibility, dependency and capacity of glucose, glutamine and fatty acid pathways in CAFs treated as indicated for 48 h ($n=3$ independent experiments). The *y* axis shows fuel oxidation, indicated by the percentage of target pathway OCR out of the OCR from all three pathways. Flexibility: $^{*}P<0.05$, $^{***}P<0.001$; dependency: $^{\dagger}P<0.05$, $^{\dagger\dagger}P<0.01$, $^{\dagger\dagger\dagger}P<0.001$; capacity: $^{\ddagger}P<0.05$; $^{\ddagger\ddagger\ddagger}P<0.001$ (when individually compared to both PBS and MCF10A/vec EV control groups). **b**, Changes of metabolite levels in the medium over 72 h by CAFs expressing anti-miR-105 or control and treated as indicated ($n=3$ independent experiments). **c**, ECAR and OCR assays in treated CAFs ($n=3$ independent experiments). *ECAR $P<0.05$, ***ECAR $P<0.001$ (when individually compared to both PBS and MCF10A/vec EV control groups). **d**, Levels of metabolites in CAFs cultured in regular medium (3 g l^{-1} glucose; 4 mM glutamine) measured by 1D NMR. Data were normalized to the PBS group ($n=3$ independent experiments). **e**,**f**, CAFs pretreated as indicated for 48 h were incubated with $^{13}C_6$–glucose (3 g l^{-1}) for 6 h in ^{12}C–glucose-free medium. Cell extracts (**e**) and the conditioned media (**f**) were analysed by 2D NMR for the abundance of ^{13}C-containing metabolites. Data were normalized to the PBS group ($n=3$ independent experiments). **g**,**h**, Pretreated CAFs were incubated with $^{13}C_5$–glutamine (4 mM) for 6 h in ^{12}C–glutamine-free medium. Cell extracts (**g**) and the conditioned media (**h**) were analysed by 2D NMR. Data were normalized to the PBS group ($n=3$ independent experiments). †undetectable. **i**, Pretreated CAFs were cultured in glucose-free medium or glutamine/glutamate-free medium for 24 h. Cell survival was determined relative to that of cells grown in regular medium. Changes of metabolite levels in the medium were also determined ($n=3$ independent experiments). For all panels, data are shown as mean ± s.d., and statistical significance was assessed using one-way ANOVA. $^{*}P<0.05$, $^{**}P<0.01$, $^{***}P<0.001$ (when individually compared to both the PBS and MCF10A/vec EV control groups) unless indicated separately. Source data are shown in Supplementary Table 5.

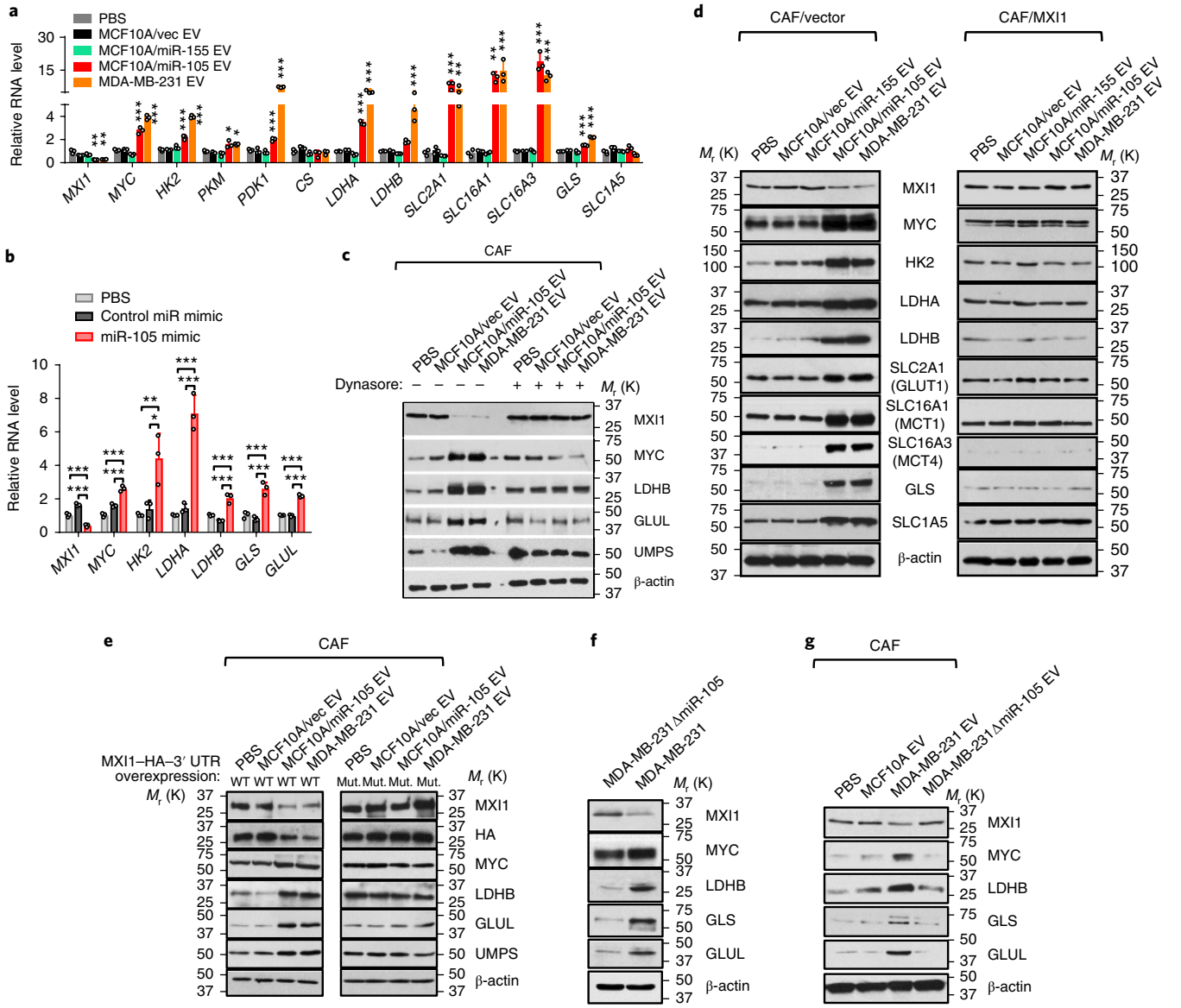

Fig. 4 | miR-105 induces genes in glucose and glutamine metabolism through targeting *MXI1*. **a**, Relative RNA levels in EV-treated CAFs were detected by RT–qPCR and compared to those for PBS-treated cells ($n=3$ independent experiments). **b**, Relative RNA levels in CAFs transfected with a miR-105 mimic, a control miRNA mimic or PBS ($n=3$ independent experiments). **c**, Western blots showing the expression levels of the indicated proteins in CAFs treated with EVs or PBS in the absence (–) or presence (+) of dynasore (10 μM). **d**, Western blots showing the expression levels of the indicated proteins in EV-treated CAFs previously transfected with an expression plasmid of *MXI1* cDNA lacking the 3′ UTR or a control vector for 16 h. **e**, Western blots showing the expression levels of the indicated proteins in EV-treated CAFs previously transfected with an expression plasmid of *MXI1* cDNA carrying the full-length WT or miR-105-site-I-mutated (Mut.) 3′ UTR. **f**, Western blots showing protein levels in WT and *miR-105*-knockout MDA-MB-231 cells. **g**, Western blots showing protein levels in CAFs treated with PBS or EVs. For all panels, the data are shown as mean ± s.d., and statistical significance was assessed using one-way ANOVA. In **a**,**b** $^{*}P<0.05$, $^{**}P<0.01$, $^{***}P<0.001$ (when individually compared to both the PBS and MCF10A/vec EV control groups unless indicated). Unprocessed original scans of blots are shown in Supplementary Fig. 9. Source data are shown in Supplementary Table 5.

(Supplementary Fig. 3a). In addition, Ingenuity Pathway Analysis predicted MYC as the top upstream regulator of miR-105-regulated genes, whereas the ENCODE chromatin immunoprecipitation (ChIP)-seq analysis identified MYC, MAX and MXI1 among the potentially involved transcription factors (Supplementary Table 2). When compared to gene expression associated with MYC overexpression, a significant subset of genes, including known MYC targets in glucose metabolism, were regulated in the same direction by miR-105 and MYC (Supplementary Fig. 3b and Fig. 1e,f), suggesting a functional overlap between miR-105 and MYC. This was confirmed by the similar capacities of miR-105 and MYC to enhance glycolysis (evidenced by an increase in ECAR and a decrease in OCR; Fig. 1g) and accelerate nutrient use (increases in the consumption of glucose and glutamine and in the production of LA and NH_4^+; Fig. 1h). Some of these effects were more pronounced when miR-105 and MYC were co-expressed. Knockdown of *MYC* expression abolished miR-105- and MYC-induced nutrient metabolism (Fig. 1h), whereas ectopic expression of MXI1 lacking the 3′ UTR abolished the induction of glycolytic genes (Fig. 1i). In contrast to the effects of miR-105 overexpression, antagonization of endogenous miR-105 increased MXI1 expression in MDA-MB-231 cells (Fig. 1j), and resembled the effects of *MYC* knockdown by reducing glucose and glutamine metabolism (Fig. 1k).

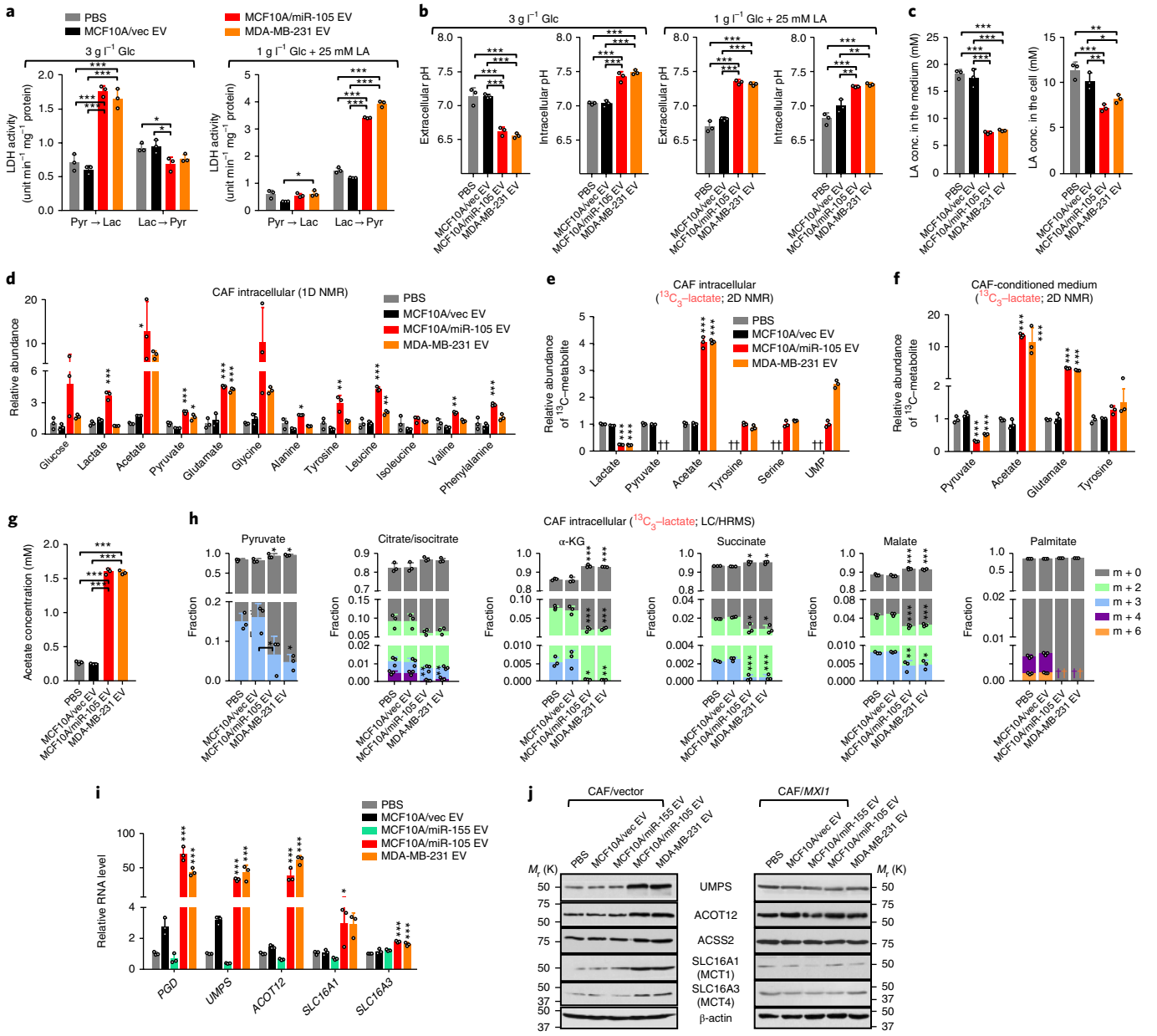

Fig. 5 | miR-105-reprogrammed CAFs have enhanced abilities to consume extracellular LA and secrete LA-derived metabolites. a, LDH activity assays to measure the interconversion between pyruvate and lactate in EV-treated CAFs under high-glucose (3 g l^{-1} glucose; no LA) or high-LA (1 g l^{-1} glucose; 25 mM LA) conditions ($n = 3$ independent experiments). **b**, Extracellular (in non-buffered conditioned medium) and intracellular pH of treated CAFs following 24 h incubation in medium containing the indicated levels of glucose and LA ($n = 3$ independent experiments). **c**, LA concentrations in the medium (10 ml medium from 10^7 cells) and in cells following 24 h incubation in medium containing 1 g l^{-1} glucose and 25 mM LA as the starting levels ($n = 3$ independent experiments). **d**, Levels of metabolites in CAFs pretreated as indicated and cultured in high-LA medium for 24 h were measured by 1D NMR. Data were normalized to the PBS group ($n = 3$ independent experiments). **e**–**h**, CAFs pretreated with EVs or PBS for 48 h were incubated in glucose-free medium containing 10 mM lactate for 24 h, and then changed to glucose-free medium containing 10 mM $^{13}C_3$-lactate. After 6 h, cell extracts (**e**,**h**) and the conditioned media (**f**,**g**; 10 ml medium from 10^7 cells) were analysed by 2D NMR (**e**,**f**; data normalized to the PBS group; $n = 3$ independent experiments), acetate assay kit (**g**; $n = 3$ independent experiments) or LC/HRMS (**h**; $n = 3$ independent experiments) for the abundances of ^{13}C-containing metabolites. †undetectable. **i**, Relative RNA levels in EV-treated CAFs grown under high-LA condition were detected by RT-qPCR and compared to those of PBS-treated cells ($n = 3$ independent experiments). **j**, Western blots showing the expression levels of the indicated proteins in EV-treated CAFs previously transfected with an expression plasmid of *MXI1* cDNA lacking the 3′UTR or a control vector for 16 h and grown under high-LA conditions. For all panels, the data are shown as mean ± s.d., and statistical significance was assessed using one-way ANOVA. $^*P < 0.05$, $^{**}P < 0.01$, $^{***}P < 0.001$ (when individually compared to both the PBS and MCF10A/vec EV control groups unless indicated). †undetectable. Unprocessed original scans of blots are shown in Supplementary Fig. 9. Source data are shown in Supplementary Table 5.

miR-105 targets *MXI1* to activate MYC signalling and is also induced by MYC. We next constructed a series of luciferase reporters containing the wild-type (WT) or mutated (ΔSite I or ΔSite II) full-length *MXI1* 3′UTR, or the annealed oligonucleotides encompassing each putative miR-105 site in the *MXI1* 3′UTR (WT or mutated; Supplementary Fig. 4a). Mutations of the highly conserved

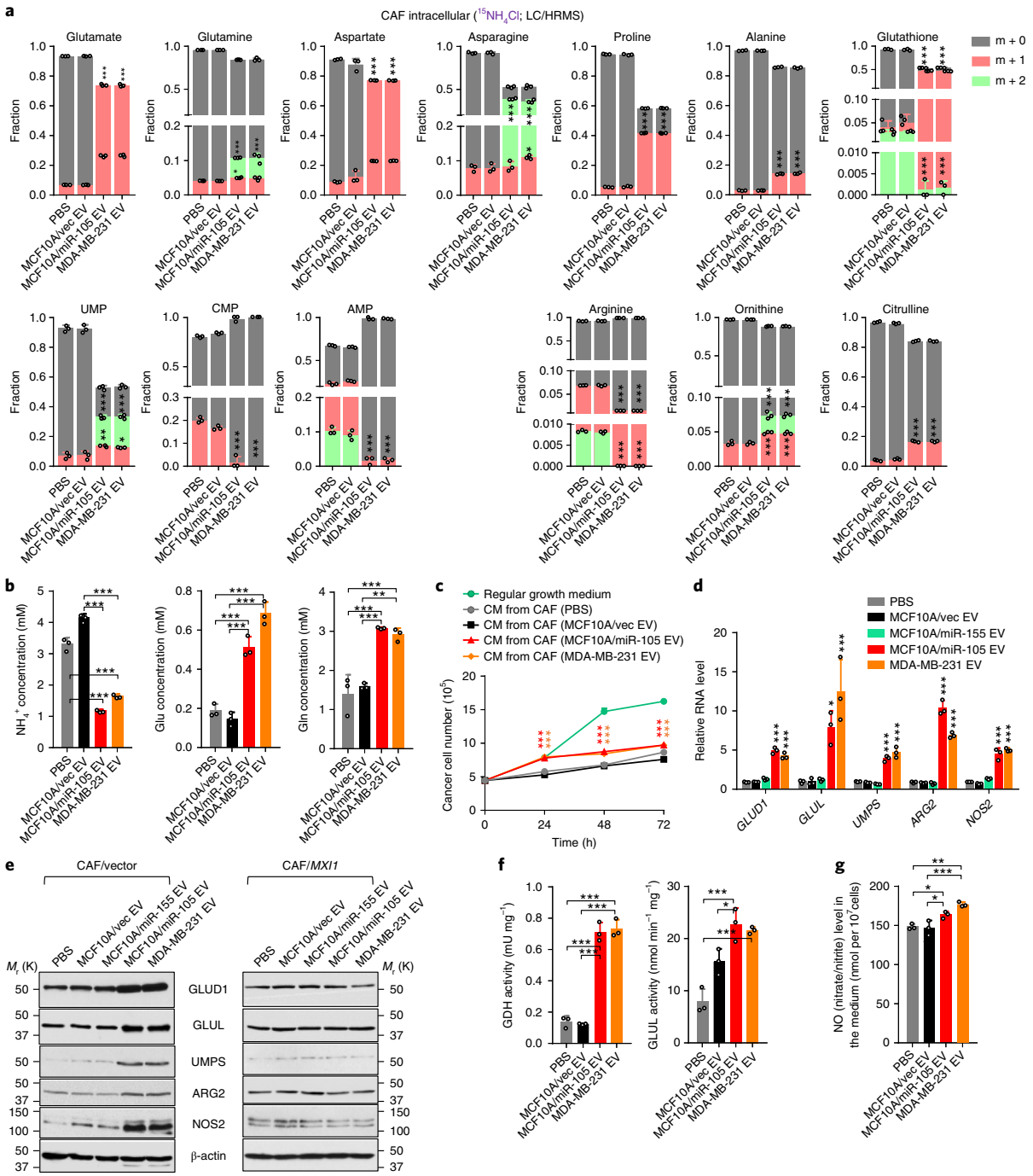

Fig. 6 | miR-105-reprogrammed CAFs have an enhanced ability to consume extracellular ammonium. a, CAFs pretreated with EVs or PBS for 48 h were incubated in glutamine/glutamate-free medium containing 5 mM $^{15}NH_4Cl$ for 16 h. Cell extracts were analysed by LC/HRMS for the abundance of ^{15}N-containing metabolites ($n = 3$ independent experiments). **b**, Concentrations of NH_4^+, glutamate and glutamine in the medium of pretreated CAFs (10 ml medium from 10^7 cells) following 24 h incubation in glutamine/glutamate-free medium containing 5 mM NH_4Cl (determined by assay kits; $n = 3$ independent experiments). **c**, MDA-MB-231 cells were cultured in regular growth medium (3 g l^{-1} glucose; 4 mM glutamine; no NH_4^+), or in NH_4^+-containing medium (3 g l^{-1} glucose; glutamine/glutamate-free; 5 mM NH_4Cl) that had been conditioned by CAFs treated as indicated. Growth of MDA-MB-231 cancer cells in the conditioned medium (CM) was determined every 24 h ($n = 3$ independent experiments). **d**, Relative RNA levels in EV-treated CAFs grown in NH_4^+-containing medium (3 g l^{-1} glucose; glutamine/glutamate-free; 5 mM NH_4Cl) were detected by RT-qPCR and compared to PBS-treated cells ($n = 3$ independent experiments). **e**, Western blots showing the expression levels of the indicated proteins in EV-treated CAFs previously transfected with an expression plasmid of *MXI1* cDNA lacking the 3′UTR or a control vector for 16 h and grown in NH_4^+-containing medium. **f**, Activities of GDH (α-KG converting to glutamate) and GLUL were measured in pretreated CAFs grown for 24 h in glutamine/glutamate-free medium containing 5 mM NH_4Cl ($n = 3$ independent experiments). **g**, Levels of NO (measured as total nitrate/nitrite by an assay kit) in the medium of pretreated CAFs following 24 h incubation in glutamine/glutamate-free medium containing 5 mM NH_4Cl ($n = 3$ independent experiments). For all panels, the data are shown as mean ± s.d., and statistical significance was assessed using one-way ANOVA. $^*P < 0.05$, $^{**}P < 0.01$, $^{***}P < 0.001$ (when individually compared to both the PBS and MCF10A/vec EV control groups unless indicated). Unprocessed original scans of blots are shown in Supplementary Fig. 9. Source data are shown in Supplementary Table 5.

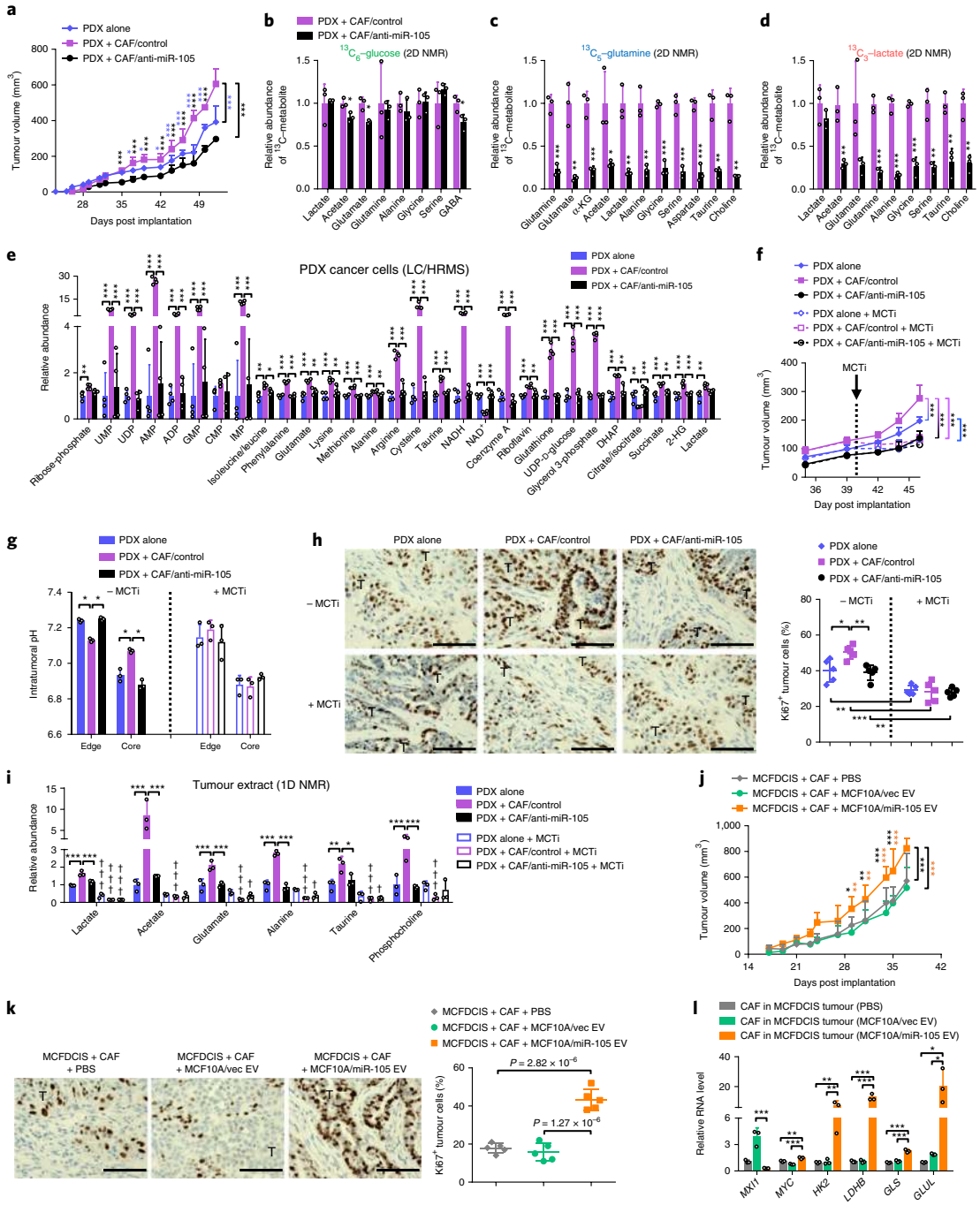

Fig. 7 | Cancer-secreted miR-105 enhances cancer–stroma metabolic coupling and promotes tumour growth. a, Female NSG mice received a mammary fat pad injection of 2×10^5 PDX BC cells, either alone or mixed with 10^6 CAFs stably expressing anti-miR-105 or control. The tumour volume was measured (two-way ANOVA, $n=7$ mice per condition). **b–d**, Tumour-bearing mice were infused with $^{13}C_6$–glucose (**b**) or $^{13}C_5$–glutamine (**c**) for 30 min, or injected with $^{13}C_3$–lactate (**d**) into the tumour. Mice were euthanized after 1 h and the tumours were collected. Abundances of ^{13}C-containing metabolites were measured by 2D NMR. Data were normalized to the PDX + CAF/control group (two-sided *t*-test, $n=3$ mice per condition). **e**, PDX cancer cells isolated from tumours were analysed by LC/HRMS for the levels of metabolites (data normalized to the PDX-alone group; one-way ANOVA, $n=4$ mice per condition). **f**, Mice were randomized within individual groups and treated with an MCT inhibitor (MCTi) or vehicle starting on day 40. Tumour volume was recorded (two-way ANOVA, $n=6$ mice per condition). **g**, Tumours from **f** were collected on day 46. Intratumoral pH in the edge and core areas of harvested tumours was measured (one-way ANOVA, $n=3$ mice per condition). **h**, Representative IHC images showing Ki67 staining and the overall percentage of Ki67$^+$ tumour cells (one-way ANOVA, $n=5$ mice per condition). Scale bars, 100 µm. **i**, Tumours from **f** were extracted for 1D NMR metabolic analysis (one-way ANOVA, $n=3$ mice per condition). $^{\dagger}P<0.05$, $^{\dagger\dagger}P<0.01$, $^{\dagger\dagger\dagger}P<0.001$ compared to the corresponding MCTi-free group. **j**, Female NSG mice received a mammary fat pad injection of 10^5 MCFDCIS cells mixed with 10^6 CAFs pretreated with EVs or PBS. Mice continued to receive EV or PBS treatment at the tumour site twice a week until tumour collection. The tumour volume was measured (two-way ANOVA, $n=6$ mice per condition). **k**, Representative IHC images showing Ki67 staining and the overall percentage of Ki67$^+$ tumour cells (one-way ANOVA, $n=5$ mice per condition). T, tumour. Scale bars, 100 µm. **l**, CAFs isolated from tumours were analysed by RT-qPCR for gene expression (one-way ANOVA, $n=3$ mice per condition). For all panels, the data are shown as mean ± s.d.; $^*P<0.05$, $^{**}P<0.01$, $^{***}P<0.001$. Source data are shown in Supplementary Table 5.

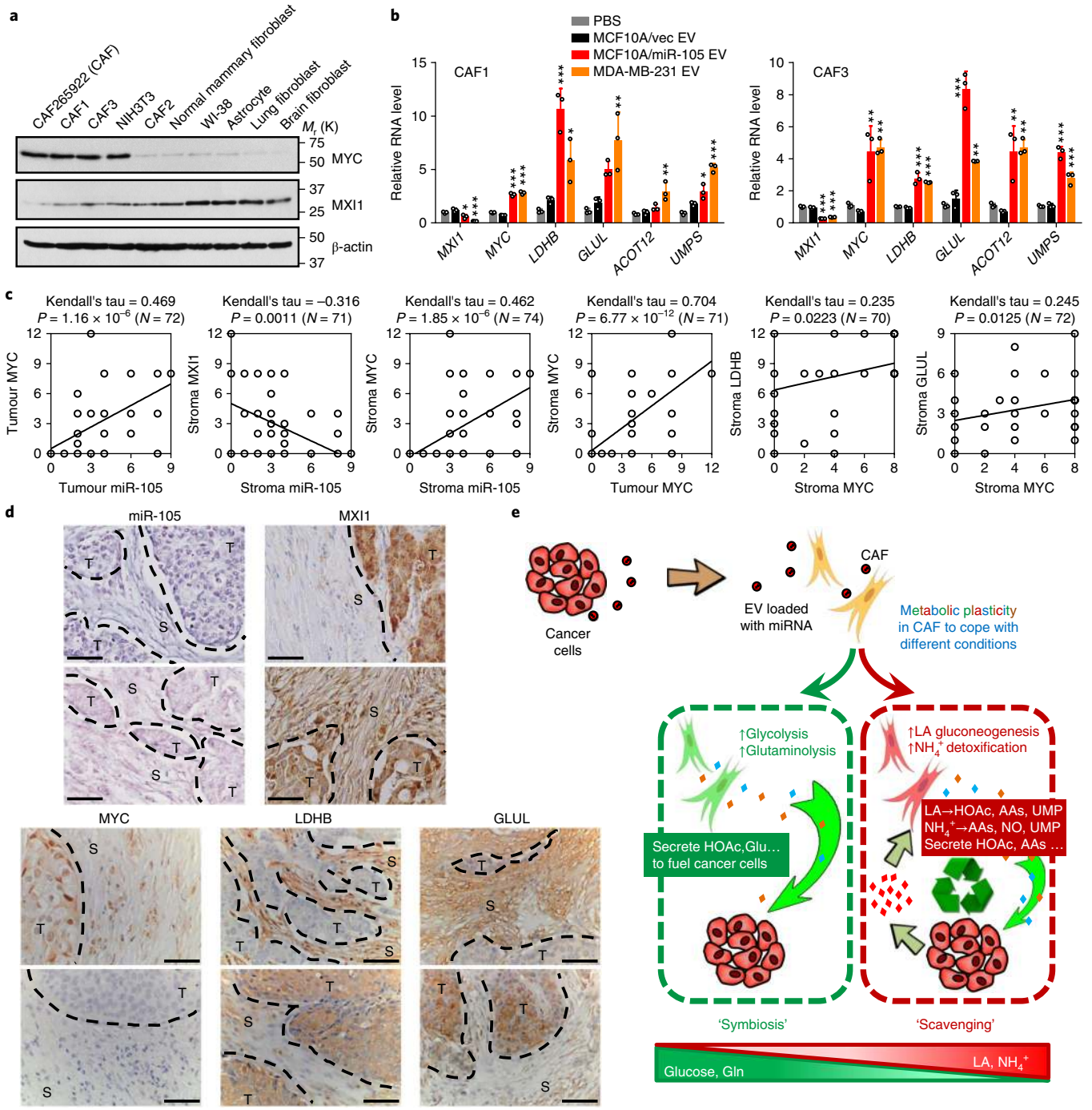

Fig. 8 | miR-105 is associated with the MYC pathway in primary tumours. a, Western blots showing protein levels of MYC and MXI1 in primary CAFs isolated from triple-negative BCs (CAF265922, the CAFs used in this study, and CAF1) and HER2$^+$ BCs (CAF2 and CAF3) and the other indicated primary cells and cell lines. **b**, Relative RNA levels in EV-treated CAF1 and CAF3 fibroblasts were detected by RT–qPCR and compared to PBS-treated cells (one-way ANOVA, $n=3$ independent experiments). Data are shown as mean ± s.d.; $^*P<0.05$, $^{**}P<0.01$, $^{***}P<0.001$ (when individually compared to both the PBS and MCF10A/vec EV control groups). **c**, A BC tissue array was analysed for correlations among selected gene expression patterns by IHC/in situ hybridization-determined scores. Correlations between nuclear MYC and miR-105 staining in tumour cells, miR-105 and MXI1 staining in the stroma, miR-105 and nuclear MYC staining in the stroma, nuclear MYC staining in the tumour and stroma, nuclear MYC and LDHB staining in the stroma, and nuclear MYC and GLUL staining in the stroma are shown. The Kendall's tau, sample size (N; number of independent tissue samples) and P value (two-sided) are indicated. **d**, Representative in situ hybridization and IHC images showing staining in tumour (T) and stroma (S). The staining was repeated twice independently with similar results. Scale bar, 100 μm. **e**, A proposed model of the metabolic reprogramming of CAFs by cancer-secreted EVs through a miR-105-mediated mechanism identified herein. Unprocessed original scans of blots are shown in Supplementary Fig. 9. Source data are shown in Supplementary Table 5.

proximal miR-105-binding site (Site I), but not Site II, abolished the responsiveness of the reporters to miR-105 (Fig. 2a). Supporting the hypothesized function of miR-105 to activate MYC through targeting *MXI1*, miR-105 induced an E-box-driven luciferase reporter, which was abolished by ectopic expression of MXI1 lacking the 3′ UTR (Fig. 2b).

In CAFs treated with MDA-MB-231 EVs, we detected an increase in miR-105, which was partially reduced by an RNA polymerase II inhibitor (Fig. 2c). This suggests that EV-transferred miR-105 may further induce the endogenous miR-105 expression in recipient CAFs to augment the effect. A thorough search of the promoter of *GABRA3*, the hosting gene harbouring *hsa-mir-105-1/2*, revealed the presence of an E-box that responded to MYC to activate reporter gene expression (Supplementary Fig. 4b and Fig. 2d). Ectopic expression of MYC indeed increased miR-105, both inside the cells and in EVs (Fig. 2e), whereas *MYC* knockdown decreased intracellular and secreted miR-105 in BC cells expressing high levels of endogenous miR-105 (Fig. 2f). We therefore proposed a MYC–miR-105–MYC activation loop, whereby the high MYC activity in cancer cells leads to a high secretion level of miR-105 to activate MYC signalling in stromal cells, phenotypically extending the effects of MYC originating from cancer cells. BC cells expressing higher levels of MYC indeed tend to secrete higher levels of miR-105 (Fig. 2g,h). EVs from these cells, but not cells with low MYC expression and low miR-105 secretion, were able to downregulate MXI1 and induce MYC and target genes in recipient CAFs (Fig. 2i).

miR-105 enhances glycolysis and glutaminolysis in CAFs. We went on to determine changes in bioenergetics, a major cellular process regulated by MYC[23,34], in CAFs following treatment with high-miR-105 EVs (from MCF10A/miR-105 and MDA-MB-231 cells) compared to low-miR-105 EV (from MCF10A/vec control cells) and PBS treatments. Comparing the use among three mitochondrial fuels, miR-105-reprogrammed CAFs exhibited reduced dependency and enhanced flexibility to oxidize glucose and glutamine, with less significant alterations with the fatty acid pathway (Fig. 3a). In a miR-105-dependent manner, the EV-reprogrammed CAFs as well as NIH3T3 cells both significantly increased the catabolism of glucose and glutamine, resulting in accelerated extracellular acidification (Fig. 3b,c and Supplementary Fig. 5a,b). In contrast, miR-155, which is also highly secreted by MDA-MB-231 cells[11] (Supplementary Fig. 2e) and used as a control here, did not significantly influence cell metabolism of glucose and glutamine (Fig. 3b,c). Nuclear magnetic resonance (NMR) spectral profiling revealed higher intracellular levels of lactate, acetate and glutamate in both fibroblast models following EV transfer of miR-105 (Fig. 3d and Supplementary Fig. 5c).

To define nutrient-specific metabolic flows, we incubated EV-pretreated CAFs with ^{13}C-labelled glucose or glutamine and measured labelled metabolites by two-dimensional (2D) NMR spectroscopy. Higher levels of ^{13}C-containing lactate, acetate, pyruvate and several amino acids were detected in miR-105-reprogrammed CAFs following ^{13}C–glucose incubation (Fig. 3e). Of particular interest, these CAFs also secreted higher amounts of labelled metabolites, especially lactate and acetate (Fig. 3f), which could potentially benefit adjacent cancer cells. Incubation with ^{13}C–glutamine resulted in increased levels of labelled glutamate, acetate, lactate and pyruvate in reprogrammed CAFs (Fig. 3g). Among these metabolites, labelled glutamate and acetate exhibited remarkably increased secretion by CAFs and could be involved in fuelling cancer cells (Fig. 3h). Thus, simultaneous induction of glycolysis and glutaminolysis in CAFs may enhance the flexibility to use either nutrient as the major fuel source. This was confirmed by the enhanced ability of reprogrammed CAFs to survive under single-nutrient deprivation of either glucose or glutamine/glutamate by increasing the use of the alternative nutrients (Fig. 3i).

The altered patterns of glucose and glutamine metabolism could be explained at the gene expression level, where genes coding for key enzymes in glycolysis (*HK2*, *LDHA*, *LDHB* and so on) and glutaminolysis (*GLS*) and for metabolite transportation (*SLC2A1*, *SLC16A1*, *SLC16A3* and *SLC1A5*) were upregulated in fibroblasts reprogrammed by high-miR-105 EVs (Fig. 4a and Supplementary Fig. 5d,e). These genes could also be induced by a synthetic miR-105 mimic (Fig. 4b) and are known MYC targets. Their regulation by high-miR-105 EVs was abolished by treating CAFs with an EV uptake inhibitor (Fig. 4c), and by expressing MXI1 lacking the 3′UTR or carrying a miR-105-site-I-mutated 3′UTR, but not MXI1 carrying the WT 3′UTR (Fig. 4d,e). Furthermore, MDA-MB-231 cells with *miR-105* gene knockout, which exhibited a higher MXI1 level and suppressed expression of MYC targets, failed to influence miR-105-regulated genes in CAFs via secreted EVs (Supplementary Fig. 4c and Fig. 4f,g).

miR-105 enables detoxification of LA and NH_4^+ by CAFs. The tetrameric enzyme lactate dehydrogenase (LDH) catalyses the interconversion between pyruvate and lactate in a tissue- and substrate-dependent manner. Elevated expression of both LDHA and LDHB in miR-105-reprogrammed fibroblasts therefore enhanced the reaction in both directions, leading to increased LA production under high glucose and increased pyruvate production under high LA (Fig. 5a and Supplementary Fig. 6a). This was accompanied by glycolysis-associated extracellular acidification but also alleviation of extreme lactic acidosis partially through the consumption of extracellular LA (Fig. 5b,c and Supplementary Fig. 6b). Under a high level of LA, miR-105-reprogrammed fibroblasts contained higher intracellular levels of acetate and glutamate (Fig. 5d), exhibited enhanced growth (Supplementary Fig. 6c) and conditioned the medium to enhance cancer cell survival (Supplementary Fig. 6d). By incubating CAFs with ^{13}C–lactate and profiling metabolites using 2D NMR and liquid chromatography coupled to high-resolution mass spectrometry (LC/HRMS), we detected increased ^{13}C-containing acetate, amino acids and UMP but decreased tricarboxylic acid intermediates and fatty acids in the cells, along with higher secretion levels of acetate and glutamate (Fig. 5e–h). CAFs reprogrammed by miR-105 increased the expression of *ACOT12* (but not *ACSS2*), *SLC16A1/3*, *PGD* and *UMPS* in a MXI1-dependent manner (Fig. 5i,j), which may respectively explain increased acetate production and secretion and suggest enhanced flow of lactate-derived gluconeogenesis into the pentose phosphate shunt for UMP biosynthesis.

We next examined the ability of EV-treated CAFs to cope with another extreme condition in glutamine/glutamate-depleted, NH_4^+-containing medium. miR-105-reprogrammed CAFs significantly increased the conversion of inorganic $^{15}NH_4^+$ into several amino acids (especially glutamate and aspartate) and into UMP (but not other nucleotides), along with enhanced arginine hydrolysis evidenced by decreased arginine and increased ornithine and citrulline containing the ^{15}N tracer (Fig. 6a). De novo glutathione synthesis was also altered, with the m+1 form dominating in miR-105-reprogrammed CAFs. This could be related to altered oxidative stress and/or redox regulation in the reprogrammed CAFs, where reduced levels of reactive oxygen species were detected (Supplementary Fig. 7a). Reprogrammed CAFs significantly enhanced the clearance of extracellular NH_4^+, and increased the secretion of glutamate as well as glutamine, which has previously been reported to fuel glutamine-addicted cancer cells[35,36] (Fig. 6b). Indeed, BC cells exhibited enhanced growth and migration in glutamine/glutamate-depleted, NH_4^+-containing media that have been conditioned by miR-105-reprogrammed CAFs (Fig. 6c and Supplementary Fig. 7b). Increased and MYC-mediated expression of *GLUD1*, *GLUL* (as previously reported[35,37]), *UMPS*, *ARG2* and *NOS2* (Fig. 6d,e), along with increased enzymatic activities of GDH and GLUL (Fig. 6f) and increased nitric oxide (NO) production (Fig. 6g), were detected in miR-105-reprogrammed CAFs. These genes control the de novo synthesis of glutamate and glutamine from NH_4^+, UMP synthesis, arginine hydrolysis and inducible synthesis of NO, respectively. It is noted that the upregulation of *GLUD1* is specific to the stress condition, as the gene was instead downregulated in miR-105-reprogrammed

CAFs cultured under growth conditions (Supplementary Fig. 7c). Thus, our results collectively indicate a detoxifying function of miR-105-reprogrammed CAFs under extreme metabolic conditions including high levels of extracellular LA and NH_4^+.

Reprogrammed CAFs assist tumour growth. To determine whether miR-105-mediated CAF reprogramming contributes to tumour growth in vivo, we orthotopically transplanted patient-derived BC cells (PDX) that were developed from the same tumour as CAFs[29] and that secreted a high level of miR-105, together with CAFs stably expressing anti-miR-105 or a control sequence, into female NOD/SCID/IL2Rγ-null (NSG) mice. Compared to transplanting cancer cells alone, co-transplantation with the control CAFs, but not with those expressing anti-miR-105, significantly enhanced tumour growth (Fig. 7a). Homogenized tumour tissues were analysed by 2D NMR following individual administration of ^{13}C-labelled tracers, including glucose and glutamine that were intravenously injected over a 30-min period and lactate injected directly into the centre of tumours. Compared to tumours containing WT CAFs, those with miR-105-resistant CAFs had lower amounts of labelled acetate and glutamate following ^{13}C–glucose injection (Fig. 7b), broad inhibition of a panel of labelled metabolites including α-KG, acetate and multiple amino acids following ^{13}C–glutamine injection (Fig. 7c), and lower amounts of labelled acetate and amino acids following ^{13}C–lactate injection (Fig. 7d). When cancer cells were purified following tumour dissociation and analysed by LC/HRMS, those from tumours containing WT CAFs contained higher amounts of biosynthesis precursors including nucleotides, amino acids, NADH and glutathione (Fig. 7e).

As acetate stood out as a common mediator of the metabolic coupling between CAFs and cancer cells in our in vitro and in vivo studies, and because the cross-plasma-membrane transport of acetate among other monocarboxylates depends on MCTs, we further determined the in vivo effect of a MCT1/2 inhibitor that was administered in established tumours. It is important to note that the MCT1/2 inhibitor would block the multi-directional transport of monocarboxylates within the tumour microenvironment, including those establishing the cancer–stroma metabolic coupling studied herein. Inhibition of MCT halted the progression of WT tumours within a week and abolished their growing advantages over those tumours with miR-105-resistant CAFs (Fig. 7f). Tumours containing WT CAFs also exhibited a less steep pH decline from the tumour edge to the core (Fig. 7g), along with increased cancer cell proliferation indicated by immunohistochemistry (IHC) of Ki67 (Fig. 7h) as well as higher levels of metabolites including lactate and acetate (Fig. 7i). These effects were all abolished by MCT inhibition.

Consistent with the findings in the PDX + CAF tumour model, co-transplantation of MDA-MB-231 cells and modified NIH3T3 cells also indicated that specifically blocking the effect of miR-105 in fibroblasts suppressed tumour growth and cancer cell proliferation (Supplementary Fig. 8a,b). In a different tumour model, we co-transplanted mice with WT CAFs and MCFDCIS cells that we have previously shown to produce a very low level of miR-105[11]. EVs with high or low miR-105 levels, or PBS as a control, were injected at the site of tumour growth to directly monitor the effect of EV-encapsulated miR-105. Compared to the other two groups, high-miR-105 EVs enhanced tumour growth and cancer cell proliferation (Fig. 7j,k), and CAFs purified from this group had lower expression of *MXI1* and higher expression of MYC-regulated metabolic genes (Fig. 7l). Collectively, the in vivo data support our hypothesis that miR-105-reprogrammed CAFs nourish cancer cells with energy-rich metabolites and contribute to sustained tumour growth.

A MYC–miR-105–MXI1–MYC loop is observed in primary tumours. Unlike lung fibroblasts and astrocytes, which reduce glucose flux by targeting the glycolytic gene *PKM* with BC-secreted miR-122[10], CAFs reprogrammed by BC-secreted EVs are highly responsive to miR-105-mediated MYC activation, inducing multiple genes involved in glucose and glutamine metabolism. We found that three out of the four cases of primary CAFs tested as well as the NIH3T3 embryonic fibroblasts expressed higher basal levels of MYC proteins compared to normal primary fibroblasts of the mammary, brain and lung as well as astrocytes, which may affect cell responsiveness to regulators of MYC activity (Fig. 8a). Furthermore, all tested mammary-derived fibroblasts had lower basal levels of MXI1, which may also sensitize the effect of an MXI1-targeting miRNA. The herein described gene regulation by EV-transferred miR-105 was also observed in other cases of CAFs from primary BCs (Fig. 8b), suggesting that the miR-105-mediated, MYC-dependent metabolic reprogramming of stromal cells is a relatively general event in BCs.

Primary human breast tumours were examined to seek evidence for the herein identified gene regulation loop consisting of the tumour-initiated MYC–miR-105 axis as well as the consequent MXI1–MYC axis extending to the stroma. In tumour cells, levels of miR-105 and nuclear-localized MYC were positively correlated, whereas in the stroma, miR-105 exhibited an inverse correlation with MXI1 and a positive correlation with nuclear MYC (Fig. 8c,d). A strong correlation between MYC levels in the tumour and stroma compartments was detected. In addition, LDHB and GLUL indeed exhibited correlations with nuclear MYC in the stroma (Fig. 8c,d).

Discussion

Altered nutrient metabolism in tumour stroma is emerging as an important aspect of cancer-associated metabolic reprogramming. Our findings collectively suggest that cancer-secreted miRNAs reprogram niche cell metabolism through various mechanisms: biasing the nutrient 'competition' toward cancer cells by suppressing the consumption of niche cells (for example, miR-122-mediated suppression of glucose uptake in lung fibroblasts and astrocytes[10]); establishing a 'symbiosis' between cancer and niche cells through which niche-produced energy-rich metabolites (acetate, glutamate and so on) feed anabolic cancer cells (shown in CAFs; Fig. 8e); and engaging 'scavengers' to support a rapidly increasing population of cancer cells by accelerating waste elimination through adjacent niche cells, which convert cancer-produced metabolic by-products into non-toxic metabolites to re-enter cancer bioenergetics (shown in CAFs; Fig. 8e). These metabolic interactions resembling those in an ecosystem may exist in different types, stages and compartments of tumours, and may depend on the metabolic pattern of cancer cells and the dynamic metabolic conditions in the tumour microenvironment. The latest findings indicate that certain tumours use lactate to fuel the tricarboxylic acid cycle[38,39] and to a certain extent can recycle ammonia into central amino acid metabolism[40]. These functions can be facilitated by CAFs through the mechanism reported herein. As CAF-derived exosomes also contain metabolic intermediates[41], we used EV-depleted CAF-conditioned media to measure the direct secretion of metabolites. We also detected glucose, lactate, acetate and glutamate in EVs derived from CAFs and epithelial cells, but at much lower levels compared to the EV-depleted medium. Beyond direct cancer–stroma metabolic interactions, reprogrammed stromal cells also exert non-metabolic effects on cancer cells, such as by inducing IL-6 production and stromal inflammation[42]. Our data suggesting altered CAF production of NO may implicate another mechanism in the associated adaptation of tumour microenvironment.

An emerging physiological significance of EVs is to transfer a 'prototype' message reflecting genetic and epigenetic alterations in donor cells (viral genome and proteins as an extreme example[43,44]) to recipient cells without these features. Some oncoproteins, oncomiRs and DNA fragments harbouring oncogenic

mutations are found in cancer-derived EVs[45–47], and may participate in transferring a cancer prototype to non-cancer cells. For instance, melanoma-derived exosomes transfer MET to bone marrow progenitors to induce a pro-metastatic phenotype[8]. EGFR-containing exosomes from gastric cancer cells influence liver stromal cells to promote liver metastasis[48]. Some glioblastomas secrete vesicles containing the tumour-specific *EGFRvIII* messenger RNA[4]. Medulloblastoma cells with *MYC* amplification secrete EVs carrying *MYC* DNA and RNA sequences[49], which could serve as an alternative mechanism to activate the MYC pathway in recipient cells. The horizontal spreading of oncogenic signals adds non-epithelial niche cells into the scenario of 'field cancerization'[50], and may underpin another advantage of targeted therapies that would also affect non-cancer cells acquiring a cancer prototype, those that are less proliferative but may serve as a 'powerhouse' and even a reservoir of oncogenic signals due to the bidirectional transfer potential of EVs.

Methods

Methods, including statements of data availability and any associated accession codes and references, are available at https://doi.org/10.1038/s41556-018-0083-6.

Received: 7 June 2017; Accepted: 8 March 2018;
Published online: 16 April 2018

References

1. Barcellos-Hoff, M. H., Lyden, D. & Wang, T. C. The evolution of the cancer niche during multistage carcinogenesis. *Nat. Rev. Cancer* **13**, 511–518 (2013).
2. Chin, A. R. & Wang, S. E. Cancer tills the premetastatic field: mechanistic basis and clinical implications. *Clin. Cancer Res.* **22**, 3725–3733 (2016).
3. Valadi, H. et al. Exosome-mediated transfer of mRNAs and microRNAs is a novel mechanism of genetic exchange between cells. *Nat. Cell. Biol.* **9**, 654–659 (2007).
4. Skog, J. et al. Glioblastoma microvesicles transport RNA and proteins that promote tumour growth and provide diagnostic biomarkers. *Nat. Cell. Biol.* **10**, 1470–1476 (2008).
5. Tkach, M. & Thery, C. Communication by extracellular vesicles: where we are and where we need to go. *Cell* **164**, 1226–1232 (2016).
6. S, E. L. A., Mager, I., Breakefield, X. O. & Wood, M. J. Extracellular vesicles: biology and emerging therapeutic opportunities. *Nat. Rev. Drug. Discov.* **12**, 347–357 (2013).
7. Becker, A. et al. Extracellular vesicles in cancer: cell-to-cell mediators of metastasis. *Cancer Cell.* **30**, 836–848 (2016).
8. Peinado, H. et al. Melanoma exosomes educate bone marrow progenitor cells toward a pro-metastatic phenotype through MET. *Nat. Med.* **18**, 883–891 (2012).
9. Webber, J., Steadman, R., Mason, M. D., Tabi, Z. & Clayton, A. Cancer exosomes trigger fibroblast to myofibroblast differentiation. *Cancer Res.* **70**, 9621–9630 (2010).
10. Fong, M. Y. et al. Breast-cancer-secreted miR-122 reprograms glucose metabolism in premetastatic niche to promote metastasis. *Nat. Cell. Biol.* **17**, 183–194 (2015).
11. Zhou, W. et al. Cancer-secreted miR-105 destroys vascular endothelial barriers to promote metastasis. *Cancer Cell.* **25**, 501–515 (2014).
12. Chow, A. et al. Macrophage immunomodulation by breast cancer-derived exosomes requires Toll-like receptor 2-mediated activation of NF-kappaB. *Sci. Rep.* **4**, 5750 (2014).
13. Redzic, J. S., Balaj, L., van der Vos, K. E. & Breakefield, X. O. Extracellular RNA mediates and marks cancer progression. *Semin. Cancer Biol.* **28**, 14–23 (2014).
14. Chin, A. R. & Wang, S. E. Cancer-derived extracellular vesicles: the 'soil conditioner' in breast cancer metastasis?. *Cancer Metast. Rev.* **35**, 669–676 (2016).
15. Costa-Silva, B. et al Pancreatic cancer exosomes initiate pre-metastatic niche formation in the liver. *Nat. Cell. Biol.* **17**, 816–826 (2015).
16. Le, M. T. et al. miR-200-containing extracellular vesicles promote breast cancer cell metastasis. *J. Clin. Invest.* **124**, 5109–5128 (2014).
17. Zhuang, G. et al. Tumour-secreted miR-9 promotes endothelial cell migration and angiogenesis by activating the JAK-STAT pathway. *EMBO J.* **31**, 3513–3523 (2012).
18. Tominaga, N. et al. Brain metastatic cancer cells release microRNA-181c-containing extracellular vesicles capable of destructing blood-brain barrier. *Nat. Commun.* **6**, 6716 (2015).
19. Wu, X. et al. De novo sequencing of circulating miRNAs identifies novel markers predicting clinical outcome of locally advanced breast cancer. *J. Transl. Med.* **10**, 42 (2012).
20. Kalluri, R. The biology and function of fibroblasts in cancer. *Nat. Rev. Cancer* **16**, 582–598 (2016).
21. Wise, D. R. Myc regulates a transcriptional program that stimulates mitochondrial glutaminolysis and leads to glutamine addiction. *Proc. Natl Acad. Sci. USA* **105**, 18782–18787 (2008).
22. DeBerardinis, R. J., Lum, J. J., Hatzivassiliou, G. & Thompson, C. B. The biology of cancer: metabolic reprogramming fuels cell growth and proliferation. *Cell. Metab.* **7**, 11–20 (2008).
23. Stine, Z. E., Walton, Z. E., Altman, B. J., Hsieh, A. L. & Dang, C. V. MYC, metabolism, and cancer. *Cancer Discov.* **5**, 1024–1039 (2015).
24. Pavlides, S. et al. The reverse Warburg effect: aerobic glycolysis in cancer associated fibroblasts and the tumor stroma. *Cell. Cycle* **8**, 3984–4001 (2009).
25. Zhang, D. et al. Metabolic reprogramming of cancer-associated fibroblasts by IDH3alpha downregulation. *Cell. Rep.* **10**, 1335–1348 (2015).
26. Lisanti, M. P., Martinez-Outschoorn, U. E. & Sotgia, F. Oncogenes induce the cancer-associated fibroblast phenotype: metabolic symbiosis and "fibroblast addiction" are new therapeutic targets for drug discovery. *Cell. Cycle* **12**, 2723–2732 (2013).
27. Martinez-Outschoorn, U. E., Lisanti, M. P. & Sotgia, F. Catabolic cancer-associated fibroblasts transfer energy and biomass to anabolic cancer cells, fueling tumor growth. *Semin. Cancer Biol.* **25**, 47–60 (2014).
28. Martins, D. et al. Loss of caveolin-1 and gain of MCT4 expression in the tumor stroma: key events in the progression from an in situ to an invasive breast carcinoma. *Cell. Cycle* **12**, 2684–2690 (2013).
29. Tsuyada, A. et al. CCL2 mediates cross-talk between cancer cells and stromal fibroblasts that regulates breast cancer stem cells. *Cancer Res.* **72**, 2768–2779 (2012).
30. Zervos, A. S., Gyuris, J. & Brent, R. Mxi1, a protein that specifically interacts with Max to bind Myc–Max recognition sites. *Cell* **72**, 223–232 (1993).
31. Schreiber-Agus, N. et al. An amino-terminal domain of Mxi1 mediates anti-Myc oncogenic activity and interacts with a homolog of the yeast transcriptional repressor SIN3. *Cell* **80**, 777–786 (1995).
32. Ayer, D. E., Lawrence, Q. A. & Eisenman, R. N. Mad-Max transcriptional repression is mediated by ternary complex formation with mammalian homologs of yeast repressor Sin3. *Cell* **80**, 767–776 (1995).
33. Lee, T. C. & Ziff, E. B. Mxi1 is a repressor of the c-Myc promoter and reverses activation by USF. *J. Biol. Chem.* **274**, 595–606 (1999).
34. Conacci-Sorrell, M., McFerrin, L. & Eisenman, R. N. An overview of MYC and its interactome. *Cold Spring Harb. Perspect. Med.* **4**, a014357 (2014).
35. Yang, L. et al. Targeting stromal glutamine synthetase in tumors disrupts tumor microenvironment-regulated cancer cell growth. *Cell. Metab.* **24**, 685–700 (2016).
36. Kung, H. N., Marks, J. R. & Chi, J. T. Glutamine synthetase is a genetic determinant of cell type-specific glutamine independence in breast epithelia. *PLoS Genet.* **7**, e1002229 (2011).
37. Bott, A. J. et al. Oncogenic Myc induces expression of glutamine synthetase through promoter demethylation. *Cell. Metab.* **22**, 1068–1077 (2015).
38. Faubert, B. Lactate metabolism in human lung tumors. *Cell* **171**, 358–371 (2017).
39. Hui, S. et al. Glucose feeds the TCA cycle via circulating lactate. *Nature* **551**, 115–118 (2017).
40. Spinelli, J.B. et al. Metabolic recycling of ammonia via glutamate dehydrogenase supports breast cancer biomass. *Science* **358**, 941–946 (2017).
41. Zhao, H. et al. Tumor microenvironment derived exosomes pleiotropically modulate cancer cell metabolism. *eLife* **5**, e10250 (2016).
42. Valencia, T. et al. Metabolic reprogramming of stromal fibroblasts through p62-mTORC1 signaling promotes inflammation and tumorigenesis. *Cancer Cell.* **26**, 121–135 (2014).
43. Booth, A. M. et al. Exosomes and HIV Gag bud from endosome-like domains of the T cell plasma membrane. *J. Cell. Biol.* **172**, 923–935 (2006).
44. Ramakrishnaiah, V. et al. Exosome-mediated transmission of hepatitis C virus between human hepatoma Huh7.5 cells. *Proc. Natl Acad. Sci. USA* **110**, 13109–13113 (2013).
45. Kahlert, C. et al. Identification of double-stranded genomic DNA spanning all chromosomes with mutated KRAS and p53 DNA in the serum exosomes of patients with pancreatic cancer. *J. Biol. Chem.* **289**, 3869–3875 (2014).
46. San Lucas, F. A. et al. Minimally invasive genomic and transcriptomic profiling of visceral cancers by next-generation sequencing of circulating exosomes. *Ann. Oncol.* **27**, 635–641 (2016).
47. Thakur, B. K. et al. Double-stranded DNA in exosomes: a novel biomarker in cancer detection. *Cell. Res.* **24**, 766–769 (2014).
48. Zhang, H. et al. Exosome-delivered EGFR regulates liver microenvironment to promote gastric cancer liver metastasis. *Nat. Commun.* **8**, 15016 (2017).
49. Balaj, L. et al. Tumour microvesicles contain retrotransposon elements and amplified oncogene sequences. *Nat. Commun.* **2**, 180 (2011).

50. Slaughter, D. P., Southwick, H. W. & Smejkal, W. Field cancerization in oral stratified squamous epithelium; clinical implications of multicentric origin. *Cancer* **6**, 963–968 (1953).

Acknowledgements

This work was supported by the National Institutes of Health (NIH)/National Cancer Institute (NCI) grants R01CA218140 (S.E.W.), R01CA166020 (S.E.W.), R01CA206911 (S.E.W.) and R01CA163586 (S.E.W.), California Breast Cancer Research Program grant 20IB-0118 (S.E.W.), Breast Cancer Research Foundation-AACR grant 12-60-26-WANG (S.E.W.) and the National Key Technology R&D Program of China Grant 2015BAI12B12 (X.R.). Research reported in this publication included work performed in Core facilities supported by the NIH/NCI under grant number P30CA23100 (UCSD Cancer Center) and P30CA33572 (City of Hope Cancer Center). We acknowledge the ENCODE Consortium and the ENCODE production laboratories generating the data sets used herein for the analysis.

Author contributions

S.E.W. and W.Y. conceived ideas, and J.W.L., Y.C. and X.R. contributed to project planning. W.Y. and S.E.W. designed and performed most of the experiments. X.W. performed all bioinformatics analyses. W.Z. performed some experiments with the MCF10A-derived lines. M.Y.F., M.C., J.W. and L.L. assisted with cell line construction and mouse experiments. Xuxiang L. and A.R.C. assisted with the nanoparticle tracking analysis and EV gradient separation. J.L., Xiaojing L. and J.W.L. performed LC/HRMS and data analysis. C.-H.C. and Y.C. assisted with NMR analysis. M.Y.F., D.P.P. and O.F. performed IHC and pathological evaluation. S.E.W. and W.Y. wrote the manuscript.

Competing interests

The authors declare no competing interests.

Additional information

Supplementary information is available for this paper at https://doi.org/10.1038/s41556-018-0083-6.

Reprints and permissions information is available at www.nature.com/reprints.

Correspondence and requests for materials should be addressed to S.E.W.

Publisher's note: Springer Nature remains neutral with regard to jurisdictional claims in published maps and institutional affiliations.

Methods

Cells and constructs. Human BC cell lines, the fetal lung fibroblast cell line WI-38 and the mouse embryonic fibroblast cell line NIH3T3 were obtained from the American Type Culture Collection and cultured in the recommended media. The non-cancerous mammary epithelial cell line MCF10A was constructed to stably overexpress miR-105 (MCF10A/miR-105), miR-155 (MCF10A/miR-155) or the empty vector (MCF10A/vec) as previously described[11]. MCF10A and derived cells were cultured as reported previously[11,51]. The patient-derived primary fibroblasts CAF265922 (denoted as CAF in the study herein) and BC cells (PDX265922, propagated in NSG mice and denoted as PDX) derived from the same triple-negative breast tumour, as well as other patient-derived primary CAFs (CAF1 from another triple-negative breast tumour; CAF2 and CAF3 from HER2$^+$ breast tumours), were isolated as previously described[29] and cultured in Iscove's modified Dulbecco's medium (Thermo Fisher Scientific) supplemented with 20% fetal bovine serum. Primary normal human mammary fibroblasts were obtained from Zen-Bio and cultured in the recommended media. Primary human astrocytes, lung fibroblasts and brain fibroblasts were obtained from ScienCell and cultured in the recommended media. All cells used herein were tested to be free of mycoplasma contamination and authenticated by using the short tandem repeat profiling method. The purity of PDX cancer cells and CAFs was ensured by fluorescence-activated cell sorting using human EpCAM as a marker for epithelial cancer cells and PDGFRβ as a marker for fibroblasts. CAFs in culture were frequently checked to confirm they were negative for EpCAM or CD31 and positive for PDGFRβ and vimentin. A lentiviral construct expressing an miArrest miR-105 inhibitor (anti-miR-105) as well as the scrambled control were purchased from GeneCopoeia to generate CAF and NIH3T3 cells with stable inhibition of miR-105 as well as the control cells. The PCR primers 5′-ATCACTCGAGAACCCAGCATGACATAAC-3′ and 5′-ATCAGCGGCCGCTTCTTCGTTCACAGTT-3′ were used to clone the WT 3′ UTR of human *MXI1*. The PCR-amplified fragments were digested with XhoI and NotI and then inserted into the same sites of the psiCHECK-2 reporter vector (Promega) downstream of the *Renilla* luciferase (Rluc) gene. The PCR primers 5′-TTGATGCAGCGGGTGATAATGAT-3′ and 5′-ATCATTATCACCCGCTGCATCAA-3′ (for mutated miR-105 binding site I; mutated nucleotides underlined), or 5′-GCTGGAAAGCGGGTGTTATAAAC-3′ and 5′-GTTTATAACACCCGCTTTCCAGC-3′ (for mutated miR-105 binding site II; mutated nucleotides underlined), were used to clone mutants of full-length *MXI1* 3′ UTR. To construct the reporters with individual miR-105 sites, annealed oligonucleotides encompassing the putative sites indicated in Supplementary Fig. 4a, either in WT or with a scrambled seed sequence, were inserted into psiCHECK-2. The *MXI1* cDNA expression plasmid was constructed by PCR cloning the full-length *MXI1* cDNA lacking the 3′ UTR using the primers 5′-ACTGGATCCATGGAGCGGGTGAAGATGA-3′ and 5′-ACTGAATTCCTATGAAGTGAATGAAAG-3′ from MCF10A cells, and inserting the open reading frame into the BamHI/EcoRI sites of the pcDNA3.1 (+) vector (Thermo Fisher Scientific). To clone the expression plasmids of *MXI1* that contains an in-frame carboxy-terminal HA tag as well as the full-length *MXI1* 3′ UTR (either WT or miR-105-site-I-mutated), the PCR-derived 3′ UTR fragments used to construct the psiCHECK-2 reporters were first inserted into the pcDNA3.1-MXI1 plasmid, downstream of the *MXI1* cDNA. Next, the primers 5′-AACATCGTATGGGTATGAAGTGAATGAAAGTTT-3′ and 5′-CCAGATTAC GCTTAGGAATTCTGCAGATATCCA-3′ were used to insert the cDNA of an in-frame HA tag immediately before the stop codon of *MXI1* through PCR with the assistance of Q5 high-fidelity DNA polymerase (New England Biolabs) following the manufacturer's protocol. The pBABE–MYC plasmid was a gift from M. Kong (University of California Irvine, USA). The promoter region (−161 to +33) of *GABRA3/hsa-mir-105/mir-767* was cloned from MCF10A cells using the PCR primers 5′-ATATATCTCGAGCAGCACAGCCGCGTGCTAAGCACCA-3′ (for the E-box-mutated promoter, the underlined 'GT' were replaced with 'TA') and 5′-GCGCGCAAGCTTCTGGTTTGCTCGCTAGCTT-3′; the PCR-amplified fragment was then ligated into the XhoI/HindIII sites of the pGL3-Basic reporter vector (Promega). The E-box luciferase reporter plasmid was constructed by inserting four tandem copies of sequence 'CACGTG' upstream of the luciferase gene in the pGL3-Promoter vector (Promega). To sequentially knock out both *hsa-mir-105-1* and *hsa-mir-105-2* genes using the CRISPR–Cas9 genomic editing system, single guide RNA (sgRNA) sequences predicted by the sgRNA Designer (https://portals.broadinstitute.org/gpp/public/analysis-tools/sgrna-design) were synthesized in DNA form and annealed into double strands, treated with T4 polynucleotide kinase and inserted into the BbsI-digested pSpCas9(BB)–2A–GFP vector[52]. The constructs were transiently transfected into MDA-MB-231 cells in combinations of two against the same gene; among the four sgRNAs designed for each gene, the combination of CAGAACCTGAGTGTGCATCG and GCTACATTGCCGTCTGCTTC was selected for *hsa-mir-105-1*, and the combination of GGTATCAGCTCATGTTGCAG and GGATGTTTGAGCATGTGCTA was selected for *hsa-mir-105-2* on the basis of their highest efficiency to induce genomic deletion of the flanking region in pilot experiments. At 24 h after transfection, GFP$^+$ cells were sorted by FACS and monoclones were screened by genotyping PCR and confirmed by sequencing (Supplementary Fig. 4c). For miR-155 overexpression, the *hsa-mir-155* gene was cloned by PCR using the primers 5′-ACAAACCAGGAAGGGGAAAT-3′ and 5′-GCAGCAATTTGTTCCATGTG-3′, and constructed into the EcoRI/SalI sites of the pBABE–GFP retroviral vector. All plasmid constructs were verified by sequencing. miScript miRNA mimics and inhibitors as well as their corresponding negative controls were purchased from Qiagen. The MYC siRNA and control siRNA were purchased from Santa Cruz Biotechnology with detailed information provided in Supplementary Table 3. Cell transfection, reporter assays, production of viruses, infection and selection of transduced cells, flow cytometry for cell characterization and Transwell migration assays were carried out as previously described[10,11,29].

EV purification and characterization. EVs secreted by cultured cells were prepared as previously reported[10,11]. Conditioned medium (CM) was first prepared by incubating cells grown at sub-confluence in growth media containing 10% EV-depleted FBS (prepared by overnight ultracentrifugation of medium-diluted FBS at 100,000*g* at 4 °C) for 48 h, and pre-cleared by centrifugation at 500*g* for 15 min and then at 10,000*g* for 20 min. EVs were isolated by ultracentrifugation at 110,000*g* for 70 min, and washed in PBS using the same ultracentrifugation conditions. When indicated, DiI (1,1′-dioctadecyl-3,3,3′,3′-tetramethylindocarbocyanine perchlorate; Sigma-Aldrich) was added into the PBS at 1 μM and incubated for 20 min before the washing spin, followed by an additional wash to remove the excess dye. The pelleted EVs were resuspended in ~100 μl of PBS, and subjected to several experiments including nanoparticle tracking analysis using a NanoSight NS300 (Malvern), iodixanol/OptiPrep gradient separation, RNA extraction by TRIZOL LS (Thermo Fisher Scientific), and treatment of cells and animals. For gradient separation, we used a protocol modified from refs[53–55]. EVs isolated by ultracentrifugation were loaded onto a 12-step OptiPrep (Sigma-Aldrich) gradient consisting of 30, 27.5, 25, 22.5, 20, 17.5, 15, 12.5, 10, 7.5, 5 and 2.5% iodixanol in 20 mM Hepes (pH 7.2), 150 mM NaCl, 1 mM Na_3VO_4 and 50 mM NaF. After centrifugation in a SW 40 Ti rotor (Beckman Coulter) at 110,000*g* at 4 °C for 16 h, twelve 1 ml fractions were collected and washed in PBS by another spin at 110,000*g* for 70 min before western analysis and RNA extraction for quantitative PCR with reverse transcription (RT–qPCR). For cell treatment, 2 μg of EVs (equivalent to those collected from ~5×10^6 producer cells) based on protein measurement using the Pierce BCA protein assay kit (Thermo Fisher Scientific) were added to 2×10^5 recipient cells. Dynasore was obtained from Sigma-Aldrich.

RNA extraction and quantitative PCR with reverse transcription. These procedures were performed as described previously[11,29]. The primers used in RT-qPCR are indicated in Supplementary Table 3. An annealing temperature of 55 °C was used for all primers. The U6 primer was used as an internal control for intracellular miRNA levels. As a spike-in control for EV miRNA levels, 20 fmol of synthetic cel-miR-39-3p was added to EVs from an equal number of cells during RNA extraction and its levels were subsequently used for data normalization following miScript miRNA RT-qPCR assays (Qiagen).

Western blot analysis. Protein extracts were separated by electrophoresis on a 10% or 12% SDS polyacrylamide gel. Protein detection was performed using the antibodies described in Supplementary Table 3.

Cell bioenergetics assays. The extracellular acidification rate (ECAR) and the oxygen consumption rate (OCR) were measured using an XF^{e}24 extracellular flux analyser (Seahorse Bioscience). Briefly, cells were seeded at 4×10^4 per well in 525 μl of XF assay medium supplemented with 2 mM glutamine (for ECAR) or 2 mM glutamine, 10 mM glucose and 1 mM pyruvate (for OCR). Cells were incubated in a CO_2-free incubator for 1 h at 37 °C to allow for temperature and pH equilibration before loading into the XF^{e}24 analyser for measurement following the manufacturer's protocol. Basal glycolysis was calculated by subtracting the third baseline (non-glycolytic acidification) ECAR reading from the third glycolysis ECAR reading following glucose addition. Basal respiration was derived by subtracting the third OCR reading following antimycin A addition from the third basal OCR reading. For the Mito Fuel Flex Test, inhibitors of glucose (UK5099), glutamine (BPTES) and fatty acid (etomoxir) pathways were applied following the manufacturer's protocol. Fuel dependency is tested by first injecting an inhibitor of the target pathway, followed by inhibition of the two alternative pathways. Fuel capacity is tested by first injecting inhibitors of the alternative pathways, followed by inhibition of the target pathway. Fuel flexibility is calculated as the difference between capacity and dependency.

Medium metabolite measurements. Cells seeded at equal number were cultured in growth media containing 3 g l^{-1} glucose but no pyruvate for 72 h before CM was collected, cleared by centrifugation and subjected to metabolite measurement using a BioProfile 100 Plus (Nova Biomedical). Medium collected from cell-free plates after 72 h incubation was used as the baseline control to calculate the consumption or production of each metabolite, which was further normalized to the cell number in each plate determined at the time of CM collection.

Intracellular and extracellular pH measurements. Cells were incubated with 5 μM of the cell-permeant pH indicator BCECF AM (2′,7′-bis-(2-carboxyethyl)-5-(and-6)-carboxyfluorescein, acetoxymethyl ester; Thermo Fisher Scientific)

in Hank's buffered salt solution (HBSS) for 25 min at 37 °C. Intracellular pH was measured by determining the ratio of fluorescence intensities at 535 nm when excited at 490 nm and 440 nm, and comparing this to a calibration curve. Extracellular pH was measured by a pH meter (Thermo Fisher Scientific).

Measurements of LDH, GDH and GLUL enzymatic activities. LDH activity was assessed using a protocol modified from a previous study[56] by measuring the reaction in two directions. The reaction of pyruvate converting to lactate was conducted at 25 °C in a mixture containing 50 mM phosphate buffer (pH 7.5), 0.18 mM NADH, 0.6 mM sodium pyruvate and cell lysate to obtain a measurable decrease in absorbance at 340 nm using a Beckman Coulter DU70 UV–Vis spectrophotometer. For the reaction of lactate converting to pyruvate, the enzymatic activity was determined by measuring an increase in absorbance at 340 nm in a reaction mixture containing 50 mM Tris-HCl buffer (pH 9.5), 50 mM lithium lactate, 0.1 mM NAD^+ and cell lysate. One unit of LDH activity was defined as the amount that consumed or produced 1 μmol of NADH per minute under the assay conditions. GDH aminating activity was assessed by adding cell lysate to a reaction mixture containing 86 mM Tris-HCl buffer (pH 8.3), 7.6 mM α-KG, 0.22 M NH_4Cl and 0.25 mM NADH. The decrease in absorbance at 340 nm was recorded at 30 °C in a spectrophotometer. Weight activity (mU mg^{-1}) was calculated by ΔOD min^{-1} for 0–5 min and normalized to cell pellet weight. One unit of GDH activity was defined as the amount that oxidized 1 μmol of NADH per minute under the conditions being analysed. GLUL activity was measured following a previously reported method[37].

Metabolic profiling by NMR spectroscopy. All NMR analyses were performed at the City of Hope NMR Core facility. Sample preparation, 1D NMR spectroscopy and data analysis were performed as described previously[10]. For experiments with ^{13}C-labelled glucose and glutamine, CAFs pretreated with EVs for 48 h were incubated with 16.6 mM (3 gl^{-1}) D-glucose–$^{13}C_6$ (≥99%; Sigma-Aldrich) in medium free of ^{12}C–glucose, or with 4 mM L-glutamine–$^{13}C_5$,$^{15}N_2$ (98%, 98%; Sigma-Aldrich) in medium free of ^{12}C–glutamine. For experiments with ^{13}C-labelled lactate, pretreated CAFs were cultured in glucose-free medium containing 10 mM lactate for 24 h, and then changed to glucose-free medium containing 10 mM sodium L-lactate–$^{13}C_3$ (≥99%; Sigma-Aldrich). The metabolic profiles of the cells were analysed after 6 h. For CM analysis, cells were washed after incubating with the tracer for 6 h, and changed to the corresponding medium containing regular unlabelled (^{12}C) metabolites; CM was collected after 24 h. To determine the abundances of ^{13}C-containing metabolites, cells and the EV-depleted CM were extracted to collect the hydrophilic fraction, which was resuspended in 500 μl of 100% D_2O containing 5 mM sodium 2,2-dimethyl-2-silapentane-5-sulfonate (Cambridge Isotope Laboratories) that serves as an internal chemical shift reference and a concentration standard in 2D spectra. NMR spectra were acquired at 25 °C on a Bruker Avance spectrometer equipped with a cryoprobe operating at 600.19 MHz ^1H frequency. One-dimensional NOESY (nuclear Overhauser effect spectroscopy) presaturation spectra[57] were collected with a spectral width of 10 kHz, 32k data points, 3 s relaxation delay and 1,024 transients. Data were processed using a Bruker topspin 3.1, and analysed with Chenomx NMR Suite Processor (version 7.5; Chenomx). Two-dimensional ^1H–^{13}C heteronuclear single quantum coherence was used to analyse cell samples and constant-time ^1H–^{13}C heteronuclear single quantum coherence was used to analyse medium and tumour samples. The spectrum widths for ^1H and ^{13}C are 16 ppm and 14 ppm, respectively. The acquisition times for ^1H and ^{13}C are 3.4 s and 122 ms, respectively. ^1H–^{13}C correlation spectra were processed using Bruker topspin 3.1, and analysed with Sparky software (T. D. Goddard and D. G. Kneller, SPARKY 3, University of California, San Francisco).

Liquid chromatography coupled to high-resolution mass spectrometry. CAFs seeded in 6-well plates at 2×10^5 cells per well were pretreated with EVs for 48 h before metabolic tracing. For lactate tracing, cells were cultured in glucose-free medium containing 10 mM lactate for 24 h, and then changed to glucose-free medium containing 10 mM sodium L-lactate–$^{13}C_3$ (≥99%; Sigma-Aldrich) for 6 h. For ammonium tracing, cells were cultured in glutamine/glutamate-free medium containing 5 mM $^{15}NH_4Cl$ (99%; Cambridge Isotope Laboratories) for 16 h. Cells were extracted and analysed by Liquid chromatography coupled to high-resolution mass spectrometry (LC/HRMS) for quantification of metabolites and mass isotopomer distributions as previously described[58], except the following modifications. Mobile phase A was replaced with water containing 5 mM ammonium acetate (pH 6.8). A scan range (m/z) of 70 to 900 was used in positive mode from 1.31 to 12.5 minutes. For negative mode, a scan range of 70 to 900 was used from 1.31 to 6.6 minutes and then 100 to 1,000 from 6.61 to 12.5 minutes. LC/HRMS-detected metabolites are summarized in Supplementary Table 4.

Measurements of metabolite levels by kits. The levels of selected metabolites were measured by commercial kits to confirm the results of metabolic profiling. These include the acetate colorimetric assay kit (BioVision), the PicoProbe lactate fluorometric assay kit (BioVision), the Glutamate-Glo assay (Promega), the glutamine colorimetric assay kit (BioVision), the EnzyChrom ammonia/ammonium assay kit (BioAssay Systems), Autokit Glucose (Wako Diagnostics) and the NO colorimetric assay kit (BioVision). The manufacturers' protocols were followed. CM-H2DCFDA was used as an indicator for reactive oxygen species following the manufacturer's protocol (Thermo Fisher Scientific).

Animals. All animal experiments were approved by the institutional animal care and use committees at the University of California San Diego and the Beckman Research Institute of the City of Hope. The study is compliant with all relevant ethical regulations regarding animal research. Female NOD/SCID/IL2Rγ-null (NSG) mice of 6–8 weeks old were used in this study. Xenograft tumours were established in NSG mice through mammary fat pad injection of 2×10^5 PDX BC cells, either alone or mixed with 1×10^6 CAFs stably expressing anti-miR-105 or control (CAF/anti-miR-105 or CAF/control), that were combined at 1:1 with Matrigel (BD Biosciences). Tumour volume was assessed by caliper measurements using the formula (width$^2\times$length)/2. A needle pH microelectrode and reference electrode (Microelectrodes) were used to measure intratumoural pH in core and periphery areas. Administration of stable isotope-labelled metabolites was performed when tumours reached ~250 mm^3. D-glucose–$^{13}C_6$ and L-glutamine–$^{13}C_5$,$^{15}N_2$ were individually administered via tail-vein infusion, whereas sodium L-lactate–$^{13}C_3$ (25 mM, 100 μl) was directly injected into the core of the tumour. For tail-vein infusion, a 27 G catheter was placed in the lateral tail vein under anesthesia. Using a syringe pump (Braintree Scientific), solutions of labelled glucose (90 gl^{-1}) or glutamine (40 mM) were infused at the speed of 700 μl h^{-1} over a total period of 30 min. Mice were euthanized 1 h after infusion/injection; tumours were collected and metabolites were extracted for 2D NMR metabolic profiling. For LC/HRMS, tumours were collected and dissociated as described[29], and sorted PDX cancer cells (previously labelled with GFP by lentiviral transduction) were analysed for the relative levels of metabolites. For the MCT inhibitor study, PDX/CAF xenograft tumours were established as described above. Mice were randomized within individual groups and started to receive the MCT1/2 inhibitor AZD3965 (100 mg kg^{-1}; orally twice a day) or vehicle on day 40. On day 46, tumour extracts were analysed for 1D NMR metabolic profiling. In another experiment, 1×10^6 MDA-MB-231 cells combined with 1×10^6 NIH3T3/anti-miR-105 or NIH3T3/control cells were injected. For the EV treatment experiment, mice were injected with 1×10^5 MCFDCIS cells mixed with 1×10^6 CAFs that had been previously treated with EVs or PBS in vitro for 2 days. The treatment with EVs or PBS continued in mice at 2 μg EVs per injection at the tumour site and twice a week starting one day after cell transplantation until tumour collection. Sorted CAFs (previously labelled with mCherry by lentiviral transduction) were analysed for gene expression.

Immunohistochemistry, in situ hybridization and immunofluorescence. BC tissue arrays were purchased from US Biomax (catalogue no. BR1505b). Immunohistochemistry (IHC) and in situ hybridization (ISH) were performed as previously described[10,11,29]. Stained slides were scored according to the intensity of staining (−: 0; +: 1; ++: 2; and +++: 3) and the percentage of the cells of interest staining positive for each antigen (0%: 0; 1~25%: 1; 26~50%: 2; 51~75%: 3; and 76~100%: 4). The intensity score was multiplied by the percentage score to obtain a final score, which was used in the statistical analyses. Immunofluorescence was performed as described previously[11]. The antibodies used are described in Supplementary Table 3.

RNA-seq and bioinformatics. RNA sequencing was performed by the City of Hope Integrative Genomics Core using RNA samples from CAFs treated with EVs derived from MDA-MB-231, MCF10A/miR-105 or MCF10A cells or with PBS, and from MCF10A cells stably overexpressing miR-105, MYC, GFP or the vector (the last two both as controls). RNA was sonicated and reverse-transcribed into cDNA, followed by end repair, A-tailing and linker ligation. The ligated material was amplified by PCR and then analysed on a HiSeq2500 (Illumina) for parallel sequencing. Sequences were aligned to human genome assembly hg19. The Bioconductor package 'edgeR' 3.4.2 was used to normalize the data and calculate the P value and $\log_2$ fold change between different groups[59]. For gene set enrichment analysis (GSEA), genes were ranked by the signed P value score, which is $-\log_{10}(P)$ with the sign of the $\log_2$ fold change. The pre-ranked data were uploaded to GSEA 3.0 and enrichment of MSigDB C2 CGP (chemical and genetic perturbation) gene sets was interrogated with 1,000 random permutations to obtain the P value, q value and normalized enrichment score NES. For Ingenuity Pathway Analysis (content version: 42012434; build: ing_pandora; Qiagen), genes altered by miR-105 overexpression in MCF10A, defined as fold change ≥2 with $P<0.05$ compared to the controls, were interrogated to predict the potential upstream regulators[60]. These genes were also interrogated by the ENCODE data sets[61] using the Enrichr online web server (2017 version)[62,63] to identify the transcription factors that could be involved in gene regulation.

Statistics and reproducibility. All quantitative data are presented as mean ± standard deviation (s.d.) unless otherwise specified. Statistical tests were performed using GraphPad Prism 7.01 and SPSS 22 unless otherwise specified. Two-sided Student's t-tests were used for comparisons of the means of data between two groups. For multiple independent groups, one-way or two-way ANOVA with post hoc Tukey tests was used. The correlations between IHC/ISH-determined gene

expression levels were evaluated by Kendall's tau correlation tests. Samples without tumour or stromal cells were removed from the correlation analysis. Values of $P < 0.05$ were considered significant. Sample size was generally chosen on the basis of preliminary data indicating the variance within each group and the differences between groups. For animal studies, sample size was predetermined to allow an 80% power to detect a difference of 50%. All samples/animals that have received the proper procedures with confidence were included for the analyses. Animals were randomized before treatments. For animal studies, the investigators were blinded to allocation during outcome assessment. All western blots were repeated independently three times with similar results, and representative images are shown. ISH and IHC staining was repeated twice independently with similar results.

Reporting Summary. Further information on experimental design is available in the the Nature Research Reporting Summary linked to this article.

Data availability. All RNA-seq data generated in this study have been deposited into the NCBI Gene Expression Omnibus (GEO) with the accession code GSE106508. The previously published GEO data set GSE50429 was reanalysed for miRNA levels in the cells and EVs of MDA-MB-231 and MCF10A (Supplementary Table 1). Previously published ENCODE ChIP-seq data that were reanalysed and shown in Supplementary Table 2 are available under the GEO accession codes GSE33213, GSE30399, GSE12782, GSE25416, GSE28286, GSE12781, GSE31363, GSE31477 and GSE32465. NMR spectrometry data for metabolic profiling have been deposited to the EMBL-EBI MetaboLights database[64] with the identifier MTBLS626 (https://www.ebi.ac.uk/metabolights/MTBLS626). Source data for Figs. 1c,f–h,j,k, 2a–f,h, 3b,c,i, 4a,b, 5a–c,g,i, 6b–d,f,g, 7a,f,g,h,j–l and 8b, and Supplementary Figs. 2a,b,d,e, 5a,b,d, 6a–d, 7a–c and 8a,b have been provided as Supplementary Table 5. All other data supporting the findings of this study are available from the corresponding author on reasonable request.

References

51. Debnath, J. et al. The role of apoptosis in creating and maintaining luminal space within normal and oncogene-expressing mammary acini. *Cell* **111**, 29–40 (2002).
52. Ran, F. A. et al. Genome engineering using the CRISPR-Cas9 system. *Nat. Protoc.* **8**, 2281–2308 (2013).
53. Tauro, B. J. et al. Comparison of ultracentrifugation, density gradient separation, and immunoaffinity capture methods for isolating human colon cancer cell line LIM1863-derived exosomes. *Methods* **56**, 293–304 (2012).
54. Kowal, J. et al. Proteomic comparison defines novel markers to characterize heterogeneous populations of extracellular vesicle subtypes. *Proc. Natl Acad. Sci. USA* **113**, 968–977 (2016).
55. Li, X. et al. Na^+–H^+ exchanger 3 (NHE3) is present in lipid rafts in the rabbit ileal brush border: a role for rafts in trafficking and rapid stimulation of NHE3. *J. Physiol.* **537**, 537–552 (2001).
56. Karamanos, Y. Purification and characterisation of lactate dehydrogenase: an undergraduate biochemistry laboratory experiment. *Adv. Biochem.* **2**, 14–23 (2014).
57. Beckonert, O. et al. Metabolic profiling, metabolomic and metabonomic procedures for NMR spectroscopy of urine, plasma, serum and tissue extracts. *Nat. Protoc.* **2**, 2692–2703 (2007).
58. Liu, X., Romero, I. L., Litchfield, L. M., Lengyel, E. & Locasale, J. W. Metformin targets central carbon metabolism and reveals mitochondrial requirements in human cancers. *Cell. Metab.* **24**, 728–739 (2016).
59. Robinson, M. D., McCarthy, D. J. & Smyth, G. K. edgeR: a Bioconductor package for differential expression analysis of digital gene expression data. *Bioinformatics* **26**, 139–140 (2010).
60. Kramer, A., Green, J., Pollard, J. & Tugendreich, S. Causal analysis approaches in Ingenuity Pathway Analysis. *Bioinformatics* **30**, 523–530 (2014).
61. Consortium, E. P. An integrated encyclopedia of DNA elements in the human genome. *Nature* **489**, 57–74 (2012).
62. Kuleshov, M. V. et al. Enrichr: a comprehensive gene set enrichment analysis web server 2016 update. *Nucleic Acids Res.* **44**, 90–97 (2016).
63. Chen, E. Y.et al. Enrichr: interactive and collaborative HTML5 gene list enrichment analysis tool. *BMC Bioinformatics* **14**, (2013).
64. Haug, K. et al. MetaboLights-an open-access general-purpose repository for metabolomics studies and associated meta-data. *Nucleic Acids Res* **41**, 781–786 (2013).

nature research

Corresponding author(s): Shizhen Emily Wang

☐ Initial submission ☐ Revised version ☒ Final submission

Life Sciences Reporting Summary

Nature Research wishes to improve the reproducibility of the work that we publish. This form is intended for publication with all accepted life science papers and provides structure for consistency and transparency in reporting. Every life science submission will use this form; some list items might not apply to an individual manuscript, but all fields must be completed for clarity.

For further information on the points included in this form, see Reporting Life Sciences Research. For further information on Nature Research policies, including our data availability policy, see Authors & Referees and the Editorial Policy Checklist.

Experimental design

1. Sample size

Describe how sample size was determined.

Sample size was generally chosen based on preliminary data indicating the variance within each group and the differences between groups. For animal studies, sample size was predetermined to allow an 80% power to detect a difference of 50%.

2. Data exclusions

Describe any data exclusions.

All samples/animals that have received the proper procedures with confidence were included for the analyses. For IHC/ISH staining of tumour tissues, samples without tumour or stromal cells were removed from the correlation analysis.

3. Replication

Describe whether the experimental findings were reliably reproduced.

All reported experimental findings were reliably reproduced in three independent experiments or by multiple biologically independent replicates.

4. Randomization

Describe how samples/organisms/participants were allocated into experimental groups.

Animals and dishes of cells were randomized before treatments.

5. Blinding

Describe whether the investigators were blinded to group allocation during data collection and/or analysis.

For animal studies, the investigators were blinded to allocation during outcome assessment.

Note: all studies involving animals and/or human research participants must disclose whether blinding and randomization were used.

6. Statistical parameters

For all figures and tables that use statistical methods, confirm that the following items are present in relevant figure legends (or in the Methods section if additional space is needed).

n/a	Confirmed	
☐	☒	The exact sample size (*n*) for each experimental group/condition, given as a discrete number and unit of measurement (animals, litters, cultures, etc.)
☐	☒	A description of how samples were collected, noting whether measurements were taken from distinct samples or whether the same sample was measured repeatedly
☐	☒	A statement indicating how many times each experiment was replicated
☐	☒	The statistical test(s) used and whether they are one- or two-sided (note: only common tests should be described solely by name; more complex techniques should be described in the Methods section)
☒	☐	A description of any assumptions or corrections, such as an adjustment for multiple comparisons
☐	☒	The test results (e.g. *P* values) given as exact values whenever possible and with confidence intervals noted
☐	☒	A clear description of statistics including central tendency (e.g. median, mean) and variation (e.g. standard deviation, interquartile range)
☐	☒	Clearly defined error bars

See the web collection on statistics for biologists for further resources and guidance.

Software

Policy information about availability of computer code

7. Software

Describe the software used to analyze the data in this study.	SPSS 22; GraphPad Prism 7.01; Bruker topspin 3.1; Chenomx NMR Suite Processor 7.5; SPARKY 3; Gene set enrichment analysis (GSEA) 3.0; edgeR 3.4.2; Ingenuity pathway analysis (content version: 42012434; build: ing_pandora); Enrichr online web server (2017 version)

For manuscripts utilizing custom algorithms or software that are central to the paper but not yet described in the published literature, software must be made available to editors and reviewers upon request. We strongly encourage code deposition in a community repository (e.g. GitHub). *Nature Methods* guidance for providing algorithms and software for publication provides further information on this topic.

Materials and reagents

Policy information about availability of materials

8. Materials availability

Indicate whether there are restrictions on availability of unique materials or if these materials are only available for distribution by a for-profit company.	There are no restrictions on the availability of materials.

9. Antibodies

Describe the antibodies used and how they were validated for use in the system under study (i.e. assay and species).

For Western blots (antibody, company, cat #, dilution):
MXI1 Santa Cruz Biotechnology sc-1042 1/200
MYC Abcam ab32072 1/1000
HK2 Cell Signaling Technology #2867 1/1000
LDHA Santa Cruz Biotechnology sc-137243 1/500
LDHB Santa Cruz Biotechnology sc-100775 1/500
GLS Abcam ab156876 1/1000
GLUL Proteintech 66323-1-Ig 1/1000
GLUD1 Millipore ABN443 1/1000
UMPS Santa Cruz Biotechnology sc-135596 1/500
ACOT12 Invitrogen PA5-32152 1/1000
ACSS2 Santa Cruz Biotechnology sc-398559 1/500
GLUT1 Abcam ab137656 1/1000
MCT1 Abcam ab216628 1/1000
MCT4 Santa Cruz Biotechnology sc-50329 1/500
ARG2 Santa Cruz Biotechnology sc-374420 1/500
NOS2 Santa Cruz Biotechnology sc-7271 1/500
HA-tag Cell Signaling Technology #2367 1/1000
CD63 Santa Cruz Biotechnology sc-59286 1/500
CD9 Cell Signaling Technology #13403 1/1000
TSG101 ThermoFisher Scientific MA1-23296 1/1000
Alix Cell Signaling Technology #2171 1/1000
β-actin Sigma-Aldrich A1978 1/1000
Donkey anti-goat IgG-HRP Santa Cruz Biotechnology sc-2020 1/5000
Amersham ECL Mouse IgG, HRP-linked whole Ab (from sheep) GE Healthcare Life Sciences NA931-1ML 1/5000
Amersham ECL Rabbit IgG, HRP-linked whole Ab (from donkey) GE Healthcare Life Sciences NA934-1ML 1/5000

For Immunohistochemistry:
Ki67 Ventana 790-4286 1/1
MXI1 Abcam ab28740 1/250
MYC Abcam ab32072 1/250
LDHB Santa Cruz Biotechnology sc-100775 1/600
GLUL Thermo Fisher Scientific LF-PA0100 1/250

For Immunofluorescence:
PDGFRB Polyclonal Antibody Thermo Fisher Scientific PA5-14718 1/10
Vimentin Millipore Sigma V2258 1/50
Goat anti-Rabbit IgG (H+L) Cross-Adsorbed Secondary Antibody, Alexa Fluor 647 Thermo Fisher Scientific A-21245 2 µg/ml
Goat anti-Mouse IgG (H+L) Cross-Adsorbed Secondary Antibody, Alexa Fluor 546 Thermo Fisher Scientific A-11003 2 µg/ml

For Flow cytometry:
APC Mouse Anti-Human EpCAM BD Biosciences 347200 5 µL/reaction
CD31 (PECAM-1) Monoclonal Antibody (WM-59 (WM59)), PerCP-eFluor 710, eBioscience™ Thermo Fisher Scientific 46-0319-42 0.125 µg/test
PDGFRB Polyclonal Antibody Thermo Fisher Scientific PA5-14718 1/10
Alexa Fluor 546 goat anti-rabbit Invitrogen A11035 1/2000

Validations are based on the datasheets from the manufacturers. The same information is also included in Supplementary Table 3.

10. Eukaryotic cell lines

a. State the source of each eukaryotic cell line used.

Human BC cell lines, fetal lung fibroblast cell line WI-38, and the mouse embryonic fibroblast cell line NIH3T3 were obtained from American Type Culture Collection (Manassas, VA) and cultured in the recommended media. The non-cancerous mammary epithelial cell line MCF10A was constructed to stably overexpress miR-105 (MCF10A/miR-105), miR-155 (MCF10A/miR-155), or the empty vector (MCF10A/vec) as previously described. MCF10A and derived cells were cultured as reported. Patient-derived primary fibroblasts CAF265922 (denoted as CAF in the study herein) and BC cells (PDX265922, propagated in NSG mice and denoted as PDX) derived from the same triple-negative breast tumour, as well as other patient-derived primary CAFs (CAF1 from another triple-negative breast tumour; CAF2 and CAF3 from HER2+ breast tumours) were isolated as previously described and cultured in Iscove's modified dulbecco's media (Thermo Fisher Scientific; Waltham, MA) supplemented with 20% fetal bovine serum. Primary normal human mammary fibroblasts were obtained from Zen-Bio (Research Triangle Park, NC) and cultured in the recommended media. Primary human astrocytes, lung fibroblasts, and brain fibroblasts were obtained from ScienCell (Carlsbad, CA) and cultured in the recommended media.

b. Describe the method of cell line authentication used.

short tandem repeat profiling

c. Report whether the cell lines were tested for mycoplasma contamination.

All cells used herein were tested to be free of mycoplasma contamination.

d. If any of the cell lines used are listed in the database of commonly misidentified cell lines maintained by ICLAC, provide a scientific rationale for their use.

No cell lines used in this study were found in the database of commonly misidentified cell lines that is maintained by ICLAC and NCBI Biosample.

Animals and human research participants

Policy information about studies involving animals; when reporting animal research, follow the ARRIVE guidelines

11. Description of research animals

Provide details on animals and/or animal-derived materials used in the study.

Female NOD/SCID/IL2Rγ-null (NSG) mice of 6-8 week old (median age 7 week) were used in this study. The body weight was 21-23 gram (median weight 22 gram).

Policy information about studies involving human research participants

12. Description of human research participants

Describe the covariate-relevant population characteristics of the human research participants.

The study did not involve human research participants.

nature research

Corresponding author(s): Shizhen Emily Wang

☐ Initial submission ☐ Revised version ☒ Final submission

Flow Cytometry Reporting Summary

Form fields will expand as needed. Please do not leave fields blank.

Data presentation

For all flow cytometry data, confirm that:

☒ 1. The axis labels state the marker and fluorochrome used (e.g. CD4-FITC).

☒ 2. The axis scales are clearly visible. Include numbers along axes only for bottom left plot of group (a 'group' is an analysis of identical markers).

☒ 3. All plots are contour plots with outliers or pseudocolor plots.

☒ 4. A numerical value for number of cells or percentage (with statistics) is provided.

Methodological details

5. Describe the sample preparation.	CAFs isolated and cultured as previously described (Tsuyada et al., 2012) were stained with indicated antobodies before subjected to flow cytometry.
6. Identify the instrument used for data collection.	BD FACSCanto II RUO (BD Bioscience, San Jose, CA)
7. Describe the software used to collect and analyze the flow cytometry data.	BD FACSDiva Software v8.0.1, FlowJo 7.6.2
8. Describe the abundance of the relevant cell populations within post-sort fractions.	N/A
9. Describe the gating strategy used.	We used flow cytometry beads as the compensation controls and performed gating based on the controls.

Tick this box to confirm that a figure exemplifying the gating strategy is provided in the Supplementary Information. ☒